JOURNAL OF PETROLOGY | VOLUME 53 | NUMBER 2 | PAGES 235–270 | 2012 | doi:10.1093/petrology/egr058

Geochemistry of Ocean Floor and Fore-arc Serpentinites: Constraints on the Ultramafic Input to Subduction Zones

JÁNOS KODOLÁNYI[1]*, THOMAS PETTKE[1], CARL SPANDLER[1], BALZ S. KAMBER[2] AND KATALIN GMÉLING[3]

[1]INSTITUTE OF GEOLOGICAL SCIENCES, UNIVERSITY OF BERN, CH-3012, BERN, SWITZERLAND

[2]DEPARTMENT OF EARTH SCIENCES, LAURENTIAN UNIVERSITY, SUDBURY, ON, P3E 2C6, CANADA

[3]DEPARTMENT OF NUCLEAR RESEARCH, INSTITUTE OF ISOTOPES, HUNGARIAN ACADEMY OF SCIENCES, H-1121, BUDAPEST, HUNGARY

RECEIVED SEPTEMBER 22, 2010; ACCEPTED OCTOBER 19, 2011
ADVANCE ACCESS PUBLICATION DECEMBER 18, 2011

We provide new insights into the geochemistry of serpentinites from mid-ocean ridges (Mid-Atlantic Ridge and Hess Deep), passive margins (Iberia Abyssal Plain and Newfoundland) and fore-arcs (Mariana and Guatemala) based on bulk-rock and in situ *mineral major and trace element compositional data collected on drill cores from the Deep Sea Drilling Project and Ocean Drilling Program. These data are important for constraining the serpentinite-hosted trace element inventory of subduction zones. Bulk serpentinites show up to several orders of magnitude enrichments in Cl, B, Sr, U, Sb, Pb, Rb, Cs and Li relative to elements of similar compatibility during mantle melting, which correspond to the highest primitive mantle-normalized B/Nb, B/Th, U/Th, Sb/Ce, Sr/Nd and Li/Y among subducted lithologies of the oceanic lithosphere (serpentinites, sediments and altered igneous oceanic crust). Among the elements showing relative enrichment, Cl and B are by far the most abundant with bulk concentrations mostly above 1000 $\mu g\ g^{-1}$ and 30 $\mu g\ g^{-1}$, respectively. All other trace elements showing relative enrichments are generally present in low concentrations ($\mu g\ g^{-1}$ level), except Sr in carbonate-bearing serpentinites (thousands of $\mu g\ g^{-1}$).* In situ *data indicate that concentrations of Cl, B, Sr, U, Sb, Rb and Cs are, and that of Li can be, increased by serpentinization. These elements are largely hosted in serpentine (lizardite and chrysotile, but not antigorite). Aragonite precipitation leads to significant enrichments in Sr, U and B, whereas calcite is important only as an Sr host. Commonly observed brucite is trace element-poor. The overall enrichment patterns are comparable among serpentinites from mid-ocean ridges, passive margins and fore-arcs, whereas the extents of enrichments are often specific to the geodynamic setting. Variability in relative trace element enrichments within a specific setting (and locality) can be several orders of magnitude. Mid-ocean ridge serpentinites often show pronounced bulk-rock U enrichment in addition to ubiquitous Cl, B and Sr enrichment. They also exhibit positive Eu anomalies on chondrite-normalized rare earth element plots. Passive margin serpentinites tend to have higher overall incompatible trace element contents than mid-ocean ridge and fore-arc serpentinites and show the highest B enrichment among all the studied serpentinites. Fore-arc serpentinites are characterized by low overall trace element contents and show the lowest Cl, but the highest Rb, Cs and Sr enrichments. Based on our data, subducted dehydrating serpentinites are likely to release fluids with high B/Nb, B/Th, U/Th, Sb/Ce and Sr/Nd, rendering them one of the potential sources of some of the characteristic trace element fingerprints of arc magmas (e.g. high B/Nb, high Sr/Nd, high Sb/Ce). However, although serpentinites are a substantial part of global subduction zone chemical cycling, owing to their low overall trace element contents (except for B and Cl) their geochemical imprint on arc magma sources (apart from addition of H_2O, B and Cl) can be masked considerably by the trace element signal from subducted crustal components.*

KEY WORDS: *Deep Sea Drilling Project; Ocean Drilling Program; serpentinite; subduction; trace elements*

*Corresponding author. Present address: Max Planck Institute for Chemistry, 27 Johann Joachim Becher Weg, Mainz, D-55128, Germany. Telephone: +49 6131 305 350. Fax: +49 6131 305.
E-mail: j.kodolanyi@mpic.de

INTRODUCTION

Serpentinites are hydrous rocks (H_2O contents up to 15–16 wt %; e.g. Vils *et al.*, 2008) that form through the alteration of olivine- and orthopyroxene-dominated lithologies at relatively low temperatures (usually $T < 400^{\circ}C$; e.g. Hemley *et al.*, 1977*a*; Janecky & Seyfried, 1986). They can be a major component of the upper part of the oceanic lithosphere (e.g. Carlson, 2001; Ranero & Sallarés, 2004). Dehydrating subducted serpentinites are considered to be important H_2O and trace element sources for arc magmas (e.g. Ulmer & Trommsdorff, 1995; Hattori & Guillot, 2003; Scambelluri *et al.*, 2004; Savov *et al.*, 2005*a*), and the trace element and isotope compositions of arc volcanic rocks have been interpreted to indicate the metasomatic effect of serpentinite dehydration fluids on arc magma sources (e.g. Singer *et al.*, 2007; Tonarini *et al.*, 2007; Barnes *et al.*, 2008). Although the number of studies investigating the trace element geochemistry of ocean floor and fore-arc serpentinites has increased considerably in the last decade (e.g. Alt & Shanks, 2003; Hattori & Guillot, 2003; Savov *et al.*, 2005*a*, 2007; Paulick *et al.*, 2006; Vils *et al.*, 2008), most of this work has focused on the behaviour of specific elements during serpentinization or on specific localities only. A comprehensive understanding of the geochemistry of ocean floor and fore-arc serpentinites is required to assess the effect of serpentinite dehydration on chemical cycling in subduction zones.

Most serpentinites are found along mid-ocean ridges and associated transform faults where great masses of mantle rocks can be exposed to seawater-derived fluids (e.g. Bonatti, 1976; Bideau *et al.*, 1991; Karson & Lawrence, 1997; Morishita *et al.*, 2009). Serpentinite may also form through slab-fluid infiltration into the fore-arc mantle atop subducting plates (e.g. Fryer *et al.*, 1985; Mottl *et al.*, 2004) and through the hydration of the subducting lithosphere adjacent to trenches, as a result of the faulting associated with plate bending (e.g. Ranero *et al.*, 2003; Contreras-Reyes *et al.*, 2007). The geochemistry of serpentinites may vary as a function of the geodynamic setting in which they form, owing to differences in the composition and temperature of the hydration fluids (e.g. Fryer, 2002; Mével, 2003).

Seawater-dominated hydration of mantle rocks leads to slight changes in bulk-rock Mg/Si (Snow & Dick, 1995; Niu, 2004) and to depletion in Ca (Janecky & Seyfried, 1986; Palandri & Reed, 2004), besides the addition of H_2O. The precipitation of aragonite and/or calcite upon advanced alteration can increase bulk-rock Ca contents (e.g. Seifert & Brunotte, 1996). Up to weight per cent (wt %) levels of chlorine can be incorporated into the newly forming serpentinite minerals and iowaite [$Mg_4Fe^{3+}(OH)_8OCl.2–4(H_2O)$; Kohls & Rodda, 1967; Agrinier *et al.*, 1996; Scambelluri *et al.*, 1997; Sharp & Barnes, 2004; Bonifacie *et al.*, 2008].

Serpentinites are regarded as the most important sinks of seawater B in hydrated oceanic lithosphere (e.g. Bonatti *et al.*, 1984; Agranier *et al.*, 2007; Vils *et al.*, 2008). Bulk-rock Sr, U, Pb, Li, Sb and As concentrations in recent and ancient ocean floor serpentinites are increased relative to other trace elements with similar compatibility during partial melting of the upper mantle (Burgath *et al.*, 1997; Stephens, 1997; Niu, 2004; Li & Lee, 2006; Paulick *et al.*, 2006; Agranier *et al.*, 2007; Hattori & Guillot, 2007). The light rare earth element (LREE) contents of ultramafic rocks can also increase as a result of serpentinization (Menzies *et al.*, 1993; Paulick *et al.*, 2006). Ocean floor serpentinization may also generate positive Eu anomalies in chondrite-normalized rare earth element (REE) patterns (Paulick *et al.*, 2006).

It is important to identify the major host minerals of trace elements showing enrichment in bulk serpentinites, because the stability of these phases can determine the mobility of the enriched elements during subduction-related metamorphism. Furthermore, a comparison of the trace element inventory of relic mantle minerals and the phases that replace them during hydration helps to distinguish hydration-related chemical features from those that are linked to upper mantle magmatic processes; it can also provide information about the extent and relative timing of hydration reactions. *In situ* trace element analyses of serpentinite minerals have so far focused on Li, Be, B and As. Serpentine is the primary host of the elevated B of ocean floor serpentinites (e.g. Scambelluri *et al.*, 2004; Lee *et al.*, 2008; Vils *et al.*, 2008). The Li content of serpentine varies from depleted to elevated values relative to its precursor mantle minerals (Decitre *et al.*, 2002; Vils *et al.*, 2008; Lee *et al.*, 2008). Arsenic, a fluid-mobile chalcophile element, is taken up largely by sulphides and serpentine, with oxides also hosting a minor fraction (Hattori *et al.*, 2005). Only limited data are available for the Sr content of serpentinite-forming silicate and carbonate phases (Milliken & Morgan, 1996; Morishita *et al.*, 2009), despite the fact that serpentinites often have higher bulk-rock Sr concentrations than expected from their peridotite precursors (e.g. Niu, 2004; Paulick *et al.*, 2006).

Here we present major and trace element geochemical data for serpentinites selected from drill cores of the Deep Sea Drilling Project (DSDP) and Ocean Drilling Program (ODP), to provide a comprehensive view on the chemical consequences of serpentinization and to chemically constrain the ultramafic input into subduction zones. Our samples represent two important geodynamic settings of ocean floor serpentinization (mid-ocean ridges and passive margins) and include fore-arc serpentinites, to explore the chemical differences specific to particular geodynamic settings. Our data provide (1) information on trace element behaviour during serpentinization, (2) constraints on the variability in trace element enrichment

related to the geodynamic setting in which serpentinization occurs and (3) constraints on the serpentinite-related element input into subduction zones.

SAMPLE MATERIALS

Our sample set consists of 39 samples from six localities, including mid-ocean ridges (MOR), passive margins (PaMa) and fore-arc environments. Samples were selected from DSDP and ODP core material as this represents the best internally consistent record (with respect to, for example, sampling methods, petrographic descriptions, on-board analyses) of rocks exposed on present-day ocean floors. Core photographs, macroscopic core descriptions and, where available, thin section descriptions of the DSDP and ODP samples were used to choose core intervals most representative of the drilled lithologies and covering variable but high degrees of serpentinization, as well as oxidation and veining, phenomena all considered to influence serpentinite bulk-rock geochemistry. We selected samples with high, but not complete degrees of serpentinization (>50% according to DSDP and ODP core description) so that the chemical effects of serpentinization dominate the bulk-rock chemistry but relic minerals are present, which allow reconstruction of the chemical character of the precursor rocks and, hence, the distinction between pre-serpentinization and serpentinization-related chemical features. We chose frequently occurring lithologies to better approach the bulk of the serpentinized oceanic mantle and tried to avoid rock types that, although important in the understanding of mantle hydration, are volumetrically less significant (e.g. talc-schists related to post-serpentinization high-Si metasomatism; Paulick *et al.*, 2006). For simplicity in reporting, we coded our samples as defined in Table 1 where sample details are also provided.

Different geodynamic settings are each represented by two localities. Mid-ocean ridge cores are from the Hess Deep and Mid-Atlantic Ridge 15°20'N Fracture Zone (MAR). Passive margin cores are from Newfoundland and the Iberian Abyssal Plain, whereas fore-arc serpentinites are from the Marianas (South Chamorro seamount) and Guatemala (Table 1). A brief description of the geological setting of the studied DSDP and ODP sites together with the simplified lithological columns of the studied drill holes is provided in Electronic Appendix 1 (EA1; downloadable from http://www.petrology.oxfordjournals.org/). More details on the geological setting can be obtained from the Initial Reports and Scientific Results of the DSDP and ODP Proceedings [available on-line at http://www.deepseadrilling.org/i.reports.htm (DSDP) and at http://www.odp.tamu.edu/publications/pubs.htm (ODP), respectively] and from the references provided in EA1.

ANALYTICAL METHODS

Petrography

Petrographic studies are based mainly on polarized light microscopy, complemented by back-scattered electron (BSE) imaging, X-ray element mapping and Raman spectroscopy (see below). Point counting (30 times 100 equally spaced points per sample) was performed on selected samples to determine the mineral proportions. We consider area fractions to be directly proportional to volume fractions. We note, however, that these calculations may be biased in samples with oriented anisometric minerals (S006 and S015).

Sample preparation for bulk-rock analyses

Bulk-rock major and trace element analysis was performed on 32 samples. Sample preparation of solid core materials for bulk-rock analyses started with careful chipping of the samples, using chisel jaws mounted on a vice, to obtain 2–3 mm chips of the inner parts of the core pieces ready for milling before trace element analysis by solution-based inductively coupled plasma mass spectrometry (ICP-MS). Vein-free aliquots were obtained from samples containing only a few veins of several millimetres width. Samples penetrated by a dense network (more than three veins per cm^2) of <1 mm wide veins were processed without removing the veins.

Chipping started with the removal of the outer 5–10 mm of the core pieces. The material that was chipped off was kept for major element analysis by X-ray fluorescence (XRF), but pieces with glue marks or other visible contamination were discarded. After chipping off the outer parts we continued crushing the inner parts of the cores until a 2–3 mm grain size was achieved. Chisel jaws were cleaned after each sample to avoid cross-contamination.

Material kept for XRF analyses was also used for B and Cl measurements by prompt gamma activation analysis (PGAA). The potential for contamination with respect to these elements is minimal, because the small amounts (i.e. $\ll$0·1 g) of potential contaminants on the sample surfaces were diluted by the 10–15 g of sample material that came off together with the surfaces during chipping. The validity of our approach of sample preparation for B and Cl analyses is supported (1) by the good agreement between measured bulk-rock concentrations and those calculated combining *in situ* measurement data and mineral proportions, and (2) by the good agreement of our bulk-rock results with published data on serpentinites from the same intervals of the same drill cores. For instance, Barnes & Sharp (2005), who cleaned their samples before analysis, reported 3100 μg g^{-1} total Cl content for ODP core 173-1068A-25R-2, 8a (103·5–105·5 cm), which is just above the position of our sample S016 (obtained from the same piece between 105 and 110 cm; Table 1), in which we measured 3010 μg g^{-1} Cl (see also Results section).

Table 1: Location, tectonic setting, labels, depth and major features of DSDP and ODP serpentinite core samples

Location and geodynamic setting	DSDP/ODP core number (Leg-Site-core-piece; interval)	Sample label	Depth (mbsf)[a]	Macro-scopic alteration	Colour	Macro-scopic veins	Carbonates	Notes
Mid-Atlantic ridge,	209-1270D-6R-1-6; 47-50	S010	33.4-34.2	complete	brown	yes	vein, repl.[b]	cab[c] veins not separable
15°20′N Fracture	209-1272A-2R-1-8; 47-51	S014	13.4-13.9	complete	yellow	yes	vein	cab veins not separable
Zone (mid-ocean	209-1272A-25R-2-6b; 70-71	S011	120.0-120.1	very high	green	no	no	
ridge)	209-1272A-27R-2-10; 101-103	S004	129.5-129.9	very high	bluish green	no	no	
	209-1274A-5R-1-4; 20-21.5	S001	26.5-26.6	very high	brownish green	yes	vein	cab veins not separable
	209-1274A-5R-1-5; 25-29	S009	26.6-26.7	very high	green	no	no	
	209-1274A-12R-1-2; 10-14	S003	59.5-59.6	very high	green	no	no	
	209-1274A-27R-1-7; 93-95	S002	147.0-147.1	very high	greenish grey	no	no	
Hess Deep	147-895D-2R-2-3a; 40-45	S039	17.8-18.0	very high	greenish grey	no	no	
(mid-ocean ridge)	147-895D-4R-5-1; 0-5	S025	40.7-41.5	high	green	yes	vein	
	147-895D-7R-1-20a; 118-123	S033	65.8-65.9	very high	brown	no	no	
	147-895E-1R-3-1; 5-10	S037	3.0-3.1	complete	dark grey	no	no	
	147-895E-2R-2-9a; 55-60	S034	21.7-22.2	complete	bluish grey	yes	vein	
	147-895E-7R-4-4; 40-45	S028	73.1-73.2	high	black	yes	vein	
Iberia Abyssal Plain	173-1068A-25R-2-8a; 105-110	S016	935.2-935.5	complete	green and brown	yes	no	
(passive margin)	173-1070A-10R-1-10; 130-133	S008	687.2-687.3	very high	bluish grey	no	vein	cab veins not separable
	173-1070A-10R-2-7; 65-66.5	S012	688.1-688.7	high	green	yes	vein, repl.	carbonate not separable
Newfoundland	210-1277A-9R-1-2b; 41-44	S013	171.1-171.2	complete	brown	yes	vein	carbonate not separable
(passive margin)	210-1277A-9R-2-1b; 16-18	S005	172.4	very high	yellow	yes	vein, repl	contains metagabbro vein; carbonate not separable
	210-1277A-9R-2-2a; 56-59	S015	172.8	complete	brown	yes	vein, repl	carbonate not separable
	210-1277A-9R-4-1f; 87-89	S006	175.9-176.0	complete	green	yes	vein, repl	contains metagabbro vein; carbonate not separable
	210-1277A-9R-6-1c; 85-87	S007	178.6-178.7	complete	green	yes	vein, repl	contains metagabbro vein; carbonate not separable
Mariana forearc	195-1200A-3R-1-1b; 60-65	S030	18.8-19.3	very high	greenish black	no	no	serpentinite clast
South Chamorro	195-1200A-13R-1-6b; 47-50	S038	109.2-109.5	very high	greenish black	yes	no	serpentinite clast
Seamount (forearc)	195-1200A-16R-1-11b; 110-115	S032	138.7-138.9	very high	green	yes	no	serpentinite clast
	195-1200A-17G-2-3; 65-70	S029	141.7-146.8	very high	green and brown	yes	no	serpentinite clast
	195-1200B-2W-1-8; 80-85	S035	31.5-31.6	high	grey	yes	no	serpentinite clast
	195-1200D-2H-1-; 10-15	S031	7.0-7.1		light greenish grey	no	not determined	serpentine mud + d < 2.0 mm clasts
	195-1200E-7H-CC-; 5-10	S026	32.3		light greenish grey	no	not determined	serpentine mud + d < 2.0 mm clasts
	195-1200E-10H-1-; 105-110	S027	53.5		light greenish grey	no	not determined	serpentine mud + d < 2.0 mm clasts
	195-1200E-10H-2-; 95-100	S036	54.9		light greenish grey	no	not determined	serpentine mud + d < 2.0 mm clasts
Guatemala (forearc)	84-566C-5-1-; 24-27	S022	109.3-109.4	very high	brown and grey	no	probably vein fragments	rock fragments in a compact srp matrix; cab not separable
	84-566C-6-1-1; 9-12	S021	117.3-117.6	very high	bluish grey	no	no	
	84-566C-7-CC-; 14-17	S020	128.5-128.8	very high	black	no	no	
	84-567A-17-2-; 70-73	S023	345.0-345.2		greenish grey	no	not determined	serpentine mud + clasts
	84-567A-28-1-1; 45-50	S019	465.7-466.2	very high	dark greenish grey	no	no	
	84-570-41-2-; 68-72	S024	385.5		greenish grey	no	not determined	serpentine mud + clasts
	84-570-42-2-; 31-34	S017	394.4-395.2	complete	black	yes	no	
	84-570-42-2-7; 58-63	S018	394.7-395.5	complete	black	yes	no	

a –Depth data include uncertainty caused by poor core recovery; mbsf: metres below seafloor; b – repl.: replacive; c – cab: carbonate; (see Petrography for further explanation)

Serpentine mud samples were disintegrated applying the same procedure as described above. However, for these samples the outer and inner parts of the core were not distinguished, because serpentine muds might become mixed by the coring device (Guatemala fore-arc) or by the device used for sampling the drill core (Mariana fore-arc). Before milling we removed all clasts bigger than 2 mm (2–5 clasts per sample) from the analysed Mariana fore-arc serpentine muds (which otherwise consist mostly of <1 mm sized grains). This was necessary because of the small mass of sample aliquots milled for the solution-based ICP-MS analyses (about 3 g each) relative to the mass of single clasts (up to a few tens of grams). The incorporation of a few, $d > 2$ mm clasts with compositions different from that of the serpentine mud (Savov *et al.*, 2005*b*) could have rendered trace element distributions fortuitous thereby introducing high uncertainties for the trace element data of these serpentine muds. Clasts were not removed from the analysed Guatemala fore-arc mud sample because they probably represent the unweathered precursor of what is today the host serpentine mud (Helm, 1985; EA1).

X-ray fluorescence

For bulk-rock XRF analysis, we crushed the outer core material to obtain 3–5 mm chips, which in turn were milled in a motorized tungsten carbide mill for 10 min. The mill was cleaned after each milling run by milling high-purity synthetic quartz, followed by cleaning with distilled water. Two grams of the rock powder of each sample were heated at 110°C overnight to remove moisture. Loss on ignition (LOI) was determined by keeping the samples at 1050°C for 2 h. About 1·5 g of each ignited sample were then mixed with $Li_2B_4O_7$ (Spectromelt A10^{TM}, Merck^{TM}, Germany) in a sample to flux mass ratio of 1:5, fused and quenched. Glass pills were analysed on an Axios (PANalytical, Netherlands) wavelength-dispersive XRF spectrometer (Institute of Mineralogy and Petrology, ETH Zürich, Switzerland). Acceleration voltage and beam current were 20–60 kV and 40–100 mA, respectively. The instrument was calibrated against international standard powders prepared as $Li_2B_4O_7$ discs. Accuracy was better than 5% (i.e. measured concentrations did not differ from preferred literature concentration data by more than 5%) for SiO_2, Al_2O_3, Cr_2O_3, FeO, MnO, NiO, MgO and CaO, with precisions better than 1% (EA2, p. 1).

Inductively coupled plasma mass spectrometry

For bulk-rock trace element analyses by ICP-MS, 2–3 mm fragments of the inner parts of the cores were milled gently by hand (so as not to abrade the milling device) using an agate mortar and pestle. Bulk-rock trace element analyses were performed on digested and diluted sample solutions using an X Series II (Thermo Fisher Scientific) quadrupole ICP-MS system at the Laurentian University (Sudbury, Canada), using an analytical protocol derived from that of Eggins *et al.* (1997). The analytical details (sample dilution, internal standardization, instrument calibration and corrections for oxide interferences) were reported by Babechuk *et al.* (2010).

For sample digestion, two methods were tested on international standards to ensure complete dissolution while maintaining low blank levels: closed beaker hotplate ($HF–HNO_3$, 72 h, 145°C) and bomb (steel-jacketed Teflon vessel, $HF–HNO_3$, 190°C, 72 h) digestion. Closed beaker digestion was initially preferred to bomb digestion because the latter led to higher V, As (e.g. 200–300 ng g^{-1}), Nb and W blanks (EA2, p. 2; see also Babechuk *et al.*, 2010). Also, long-term compositional data for US Geological Survey (USGS) BIR-1 and Geological Survey of Japan (GSJ) JA-3 and JP-1 standards show (EA2, p. 2) that reproducibility can be better than 2·5% (1σ) from multiple beaker digests, even for very low-abundance elements (e.g. Rb and U, both <0·2 μg g^{-1} in BIR-1). However, bomb digestion ensures complete dissolution of the sample, as illustrated by the higher concentrations of elements largely hosted by low-solubility spinel (Ti, V, Cr, Zn, Ga) in the bomb-digested aliquots of JP-1 relative to the beaker-digested aliquots (EA2, p. 2). Therefore, data obtained from the bomb-digested aliquots of our samples are used throughout.

Average trace element concentrations measured in bomb-digested aliquots of JP-1 are in good agreement with those generally reported in the literature (<12% difference between measured and preferred values; EA2). Detection limits for trace elements expected to have very low abundances in our samples (e.g. Be, Nb, Sb, Cs, REE, Pb, Th and U) were below 1 ng g^{-1} (for Cs, most REE and U as low as 0·1 ng g^{-1}; EA2). The external reproducibility for elements with concentrations <40 ng g^{-1} can be inferred from the measurements of the trace element poor JP-1 standard (EA2). The best precisions are observed for the LREE, Sb and Cs (RSD <3%), whereas measurements on Be, middle REE (MREE) and heavy REE (HREE), Th and U have higher uncertainties (RSD = 3–7%). Among the low-abundance elements Nb shows by far the poorest precision (RSD = 13%) in bomb digestions because of the relatively high and variable blank contribution.

Prompt gamma activation analysis

Bulk-rock B and Cl contents of 23 serpentinites were determined at the PGAA facility of the Budapest Research Reactor (BRR). The system has been described by Belgya & Révay (2004).

Between 0·8 and 1·6 g of the sample powder obtained for major element analysis from the exposed sample material was heated at 110°C overnight, wrapped in clean 20 mm × 30 mm × 2 mm Teflon bags and sealed.

The powder-filled bags were irradiated in a cold neutron beam (flux $1{\cdot}2 \times 108\,cm^{-2}\,s^{-1}$). The neutron flux was stable during the reactor cycles and homogeneous in the area of the beam. The emitted gamma radiation was detected with a high purity germanium detector, surrounded by a bismuth germanate scintillator (Canberra Instruments). The total number of counts on the most prominent peaks of B and Cl for each sample were between 2 500 000 and 3 000 000. The spectra were fitted with the Hypermet-PC software. We used the prompt gamma library of Révay *et al.* (2001) for element identification. Quantification was performed with an in-house Excel^{TM} macro, utilizing the k_0 standardization method (modified after Molnár *et al.*, 1998), which determines mass ratios of different elements using partial cross-section data obtained on pure elemental and compound standards with H as comparator element. Accordingly, all major and minor elements were included in data reduction. The accuracy of the method is better than 10%, as documented by Gméling *et al.* (2005), Di Nicola *et al.* (2009) and Révay (2009). Total uncertainty [estimated following the calculation scheme of Révay (2006)] was <3% for Cl and <2% for B. Detection limits were between 18 and 120 and between 0·07 and $0{\cdot}33\,\mu g\,g^{-1}$ for Cl and B, respectively.

Raman spectroscopy

We used Raman spectroscopy to constrain the serpentine mineralogy (Rinaudo *et al.*, 2003; Auzende *et al.*, 2004; Groppo *et al.*, 2006). *In situ* confocal micro-Raman spectroscopy of mineral phases was performed with a Jobin Yvon LabRAM-HR800 integrated Raman microprobe system at the University of Bern. This consists of a He–Ne internal and an Nd–YAG external laser, an Olympus BX41 microscope and an 800 mm focal length spectrograph equipped with a CCD. Green and red to brown materials were excited with 532·12 nm and 632·817 nm laser irradiation, respectively. Using a 100× objective lens allowed a spatial resolution of 5–10 μm. Spectral resolution was between 1 and $2\,cm^{-1}$.

X-ray element mapping

Element mapping was performed by wavelength-dispersive X-ray spectrometry (WDS) on a JEOL JXA 8200 electron microprobe at the University of Bern. Electron beam diameters were 1–2 μm. Dwell times on each spot were between 30 and 150 ms, depending on the analysed element and the sensitivity of the detector.

Electron probe microanalysis (EPMA)

In situ major and minor element abundances in minerals were determined by WDS using a JEOL JXA 8200 electron microprobe (University of Bern), operated at 15 kV acceleration voltage and 20 nA beam current. The beam diameter was 3 μm for all but the serpentine and brucite analyses, for which a 10 μm beam was used to avoid damage that was visible when using a 3 μm beam. Counting times were 20 s both on background and peak positions for all elements except Ni, for which the peak and background counting time was 60 s. Raw intensity data were processed using the PRZ (CITZAF) corrections and standardized using well-characterized natural and synthetic minerals chosen to match the matrix of the analysed minerals as closely as possible.

Laser ablation ICP-MS (LA-ICP-MS)

In situ trace element compositions were determined with an ELAN-DRCe ICP-MS system (Perkin Elmer, USA) coupled with a GeoLas Pro 193 nm ArF Excimer laser system (Lambda Physik, Germany) at the University of Bern. The most important analytical parameters are listed in EA2 (p. 3). Standard and sample ablation rate was set to $1{\cdot}2$–$1{\cdot}6\,\mu m\,s^{-1}$ by varying the laser energy density (3–$20\,J\,cm^{-2}$) and pulse repetition rate (7–10 Hz). Beam sizes were set between 24 and 120 μm to obtain the highest possible signals while avoiding hitting fractures or that different textural types of the same phase are included in a single analysis. ICP-MS settings were optimized to achieve maximum sensitivity at low oxide production ($^{232}Th^{16}O^{+}/^{232}Th < 0{\cdot}5\%$) and U/Th sensitivity ratios of ~1 (Günther & Hattendorf, 2005). Some analyses were performed with an admixture of H_2 to the laser aerosol gas (He) to lower the limits of detection (LOD) and uncertainties associated with low-abundance element determinations (Guillong & Heinrich, 2007).

Data reduction was done using Lamtrace (Jackson, 2008), following the basic principles of Longerich *et al.* (1996). We used synthetic glasses (SRM 610 or 612 from NIST) for external standardization applying the reference concentrations listed in EA2 (p. 4). Major element concentrations obtained by electron microprobe were used for internal standardization of silicates. Where electron microprobe data were missing from the spot where we performed the laser analysis, the internal standardization used the average major element concentration obtained on the same mineral in the same textural position and spatially the closest to the laser spot. The internal standard for carbonates was an assumed CaO (measured isotope was ^{43}Ca to avoid too high count rates) content between 54 and 56 wt %, adjusted to keep the sum of major and minor components (CaO, MgO, SrO, MnO, FeO, Na_2O and CO_2) at 100 wt %, while maintaining stoichiometry. The accuracy of measurements was monitored by repeat analyses of the NIST 612 and NIST 616 glasses as unknowns. Measured concentrations of all analysed elements differed <15% from the preferred values from the literature. External precisions, as suggested by the relative standard deviation of standard measurements are 3% for Ni, 2% for Li, B, Cr and Ba, and better than 1% for all other analysed trace elements at the 30–$40\,\mu g\,g^{-1}$ level. External precisions are poorer (mostly 10–20%) for

low-abundance (i.e. $\mu g\,g^{-1}$ concentration level) elements. Detection limits depend on laser beam size and element setup (e.g. number of elements analysed per spot). For most analyses they were $>1\,\mu g\,g^{-1}$ for Ni and Cr, $0{\cdot}1-1\,\mu g\,g^{-1}$ for Li, B and Mn, $0{\cdot}01-0{\cdot}1\,\mu g\,g^{-1}$ for As, Ba and Sb, and $<0{\cdot}01\,\mu g\,g^{-1}$ for all other analysed trace elements.

PETROGRAPHY

Mineral abbreviations used throughout are after Kretz (1983) or defined upon first use. The mineralogy and classification of the samples is given in Table 2. The results of point counting and Raman spectroscopy of selected samples are reported in Table 3.

Apart from the serpentine muds all samples investigated are strongly to completely serpentinized peridotites. They consist of 1–3 of the three serpentine minerals (chrysotile, lizardite, and antigorite), brucite, chlorite, tremolite, talc, magnetite and sometimes carbonates and sulphides, together with relic olivine ± orthopyroxene ± clinopyroxene ± spinel ± high-Al amphibole. The degree of alteration (the volumetric proportion of serpentine, brucite, talc, hydrothermal amphibole, chlorite, magnetite and carbonate in the entire rock volume without vein-fillings) varies between 69 and 100%, mostly 85–95% (Table 3). Carbonate (cab) forms veins or fills former serpentine ± brucite pseudomorphs after olivine or orthopyroxene. Sulphide (slph) crystals occur rarely. Lone 10–50 μm sulphide grains are interpreted as relics of mantle sulphides or their recrystallized or altered equivalents, whereas evenly distributed <10 μm sulphide grains are considered to be serpentinization-related. Iowaite (iow) occurs in some MAR and Hess Deep samples (Table 2). Gypsum was observed in one sample from Guatemala where it forms clusters in a mud-like serpentinite breccia.

Unlike any other sample, S021 from Guatemala bears evidence for the progressive decomposition of the ocean floor serpentinite assemblage (chrysotile + hydroxide phases + magnetite) leading to the growth of antigorite and Al-free clinopyroxene. The prograde antigorite + clinopyroxene assemblage of S021 has been discussed elsewhere (Kodolányi & Pettke, 2011).

Relic textural features

Pseudomorphic replacements after olivine and orthopyroxene allow the original modal abundances to be estimated. The protoliths were spinel-harzburgites, spinel-dunites and one olivine-websterite (Table 2), with mostly protogranular to porphyroclastic (see Mercier & Nicolas, 1975) textures (Fig. 1a).

Olivine formed 0·2–4 mm subhedral grains whereas orthopyroxene crystals were subhedral to euhedral and 1–6 mm in diameter prior to serpentinization. Clinopyroxene usually has equant crystals (Fig. 1b), appears as exsolution lamellae in orthopyroxene and sometimes occurs as stringers of interstitial (i.e. with respect to former olivine and orthopyroxene) irregularly shaped grains or vermicular intergrowths with spinel (MAR and Hess Deep). Clinopyroxene and clinopyroxene–spinel intergrowths in the MAR samples also appear along the former margins of orthopyroxene crystals. We also observed minute ($d < 10$ μm) clinopyroxene crystals, which formed through the recrystallization of clinopyroxene exsolution lamellae in orthopyroxene (S038, Mariana fore-arc). Spinel forms subhedral to euhedral isometric crystals and sometimes occurs as millimetre long elongated crystals with curvilinear grain boundaries or forms vermicular intergrowths with clinopyroxene (MAR and Hess Deep). If present, amphibole is a minor phase (less than *c.* 5 vol. %; Table 3). Amphibole not related to hydrothermal activity occurs as pargasite associated with clinopyroxene (S008, Iberia Abyssal Plain) or forms sub- to euhedral magnesio-hornblende crystals in the altered gabbro veins of some of the Newfoundland PaMa serpentinites (S005, S007). These gabbro veins are so altered that only high-Al amphibole and, where present, clinopyroxene and zircon remained intact. Gabbro veins can be accompanied by trails of magnesio-hornblende forming a network in the serpentinized peridotite matrix. In one sample (S006, Newfoundland) 200–300 μm long anthophyllite laths were identified as crystal fragments within and along the margins of a serpentine vein.

Textures related to seafloor hydration

The mineral assemblage formed by seafloor hydration consists mainly of replacive and vein serpentine. Replacive serpentine is dominated by pseudomorphic microtextures (Wicks & Whittaker, 1977).

The hydration of olivine

Olivine is replaced by serpentine ± brucite, forming a mesh-like network (mesh rims; Wicks *et al.*, 1977) around relic olivine (Fig. 1c). Where hydration of olivine is complete, the mesh centers of serpentine ± magnetite ± brucite dominate (Fig. 1d). Mesh centers can be further replaced by carbonate (replacive carbonate, calcite where mineralogy could be determined; Table 1; Fig. 1e) upon progressive alteration. The presence of brucite in mesh rims or in mesh centers can be inferred from the EPMA results (see below). Raman data identify lizardite as the most common serpentine phase in mesh rims and centers (Table 3; Fig. 1f and g). Magnetite usually forms strings of single crystals along the serpentine mesh-network (Fig. 1c–e). Magnetite also appears in brucite-poor mesh centers (Figs. 1d-e). Very rare iowaite was found in the mesh rims around relic olivine and in the serpentine ± magnetite dominated mesh centers.

Table 2: Mineralogy of DSDP and ODP serpentinites[a] and classification of their protoliths

Sample no.	Locality	Major phases[b]	Minor phases[b]	Original lithology[c]
S001	MAR	ol, srp	opx, cpx, spl, mag, arg	harzburgite
S002	MAR	srp	ol, opx, cpx, spl, mag	harzburgite
S003	MAR	opx, srp	ol, cpx, spl, brc, mag	harzburgite
S004	MAR	opx, srp	ol, cpx, spl, iow, mag	harzburgite
S009	MAR	ol, opx, srp	cpx, spl, mag, slph	harzburgite
S010	MAR	srp, arg	spl, mag	dunite
S011	MAR	opx, srp	ol, cpx, spl, brc, mag	harzburgite
S014	MAR	srp, arg	spl, mag	dunite
S025	Hess Deep	ol, srp	opx, cpx, spl, amp, mag, arg, slph	harzburgite
S028	Hess Deep	ol, opx, srp	cpx, spl, mag, slph	harzburgite
S033	Hess Deep	opx, srp	ol, cpx, spl, brc, tlc, mag, slph	harzburgite
S034	Hess Deep	srp, brc, arg	spl, mag, slph	dunite
S037	Hess Deep	srp	spl, brc, mag	dunite
S039	Hess Deep	ol, opx, srp	cpx, spl, amp, brc, iow, chl, mag, slph	harzburgite
S005	Newfoundland	amp, srp	spl, zrn, chl, mag, Mn-oxides	harzburgite (+ gabbro vein)
S006	Newfoundland	amp, srp, cal	opx, spl, chl, mag, slph	harzburgite (+ gabbro vein)
S007	Newfoundland	srp	opx, cpx, spl, amp, chl, mag, cab	harzburgite (+ gabbro vein)
S013	Newfoundland	srp	opx, spl, mag, cal, Mn-oxides	dunite
S015	Newfoundland	srp, cal	spl, amp, chl, mag	dunite
S008	Iberia	srp	opx, cpx, spl, amp, chl, mag, cal, slph	harzburgite
S012	Iberia	cpx, srp	opx, mag, cal, slph	ol-websterite
S016	Iberia	srp, chl	spl, mag, adr, slph, Mn-oxides	harzburgite
S017	Guatemala	srp	spl, mag, slph	dunite
S018	Guatemala	srp	spl, mag, slph	dunite
S019	Guatemala	srp	opx, spl, mag	harzburgite
S020	Guatemala	srp	ol, opx, cpx, spl, brc	harzburgite
S021	Guatemala	srp	ol, cpx, brc, mag, slph	harzburgite
S022	Guatemala	srp	ol, spl, mag, cal, gp	dunite[d]
S023	Guatemala	srp	spl, mag	dunite[d]
S024	Guatemala	srp	spl	harzburgite[d]
S029	Mariana	srp	ol, cpx, spl, brc, mag	dunite[d]
S030	Mariana	opx, srp	ol, cpx, spl, brc, chl, mag	harzburgite[d]
S032	Mariana	srp	ol, opx, cpx, spl, amp, mag	harzburgite[d]
S035	Mariana	ol, opx, srp	cpx, spl	harzburgite[d]
S038	Mariana	opx, srp	ol, cpx, spl, brc, tlc, mag	harzburgite[d]

[a]Serpentine muds of ODP Leg 195 (Mariana FA) are not listed.
[b]Determined by micropetrography, BSE imaging and element mapping.
[c]Estimated on the basis of micropetrographic observations.
[d]Lithology of the clast(s).

The hydration of orthopyroxene

Hydration of orthopyroxene is pseudomorphic. Pseudomorphic silicate replacements after orthpyroxene are referred to as bastite (Fig. 2a and b). Bastite generally consists of lizardite and rarely of chrysotile (Table 3). Talc associated with bastite is present in only two samples (S033 and S038, from the Hess Deep and the Mariana fore-arc, respectively), where it forms coronas around bastite and orthopyroxene. Magnetite associated with bastite is present only in strongly altered rocks. Bastite grains look relatively uniform within a single sample, although there can be differences regarding colour (e.g. in S017, from the Guatemala fore-arc, where colourless and green bastite varieties are present). Carbonate (calcite where the

Table 3: Mineral proportions[a] and serpentine polymorphs of selected DSDP and ODP serpentinites

Locality	Mid-Atlantic ridge (mid-ocean ridge)						Hess Deep (mid-ocean ridge)			
Sample no.	S001	S003	S004	S009	S011	S014	S025	S033	S034	S039
Mineral proportions [surface %]										
ol	12.2	4.9	4.2	11.0	0.3		24.0	3.7	0.0	8.2
opx	3.6	6.4	6.8	7.9	0.1		1.1	5.7	0.0	7.3
cpx	3.3	0.8	0.1	0.3	trace		1.0	1.8	0.0	0.6
spl	4.0	0.9	0.1	0.6	1.8		0.3	0.3	0.7	0.5
amp	0.0	0.0	0.0	0.0	0.0		trace	0.0	0.0	trace
mesh rims and centers[b]	46.9	68.1	69.9	58.2	63.4		35.6	71.0	86.1	72.0
bastite[c]	14.0	10.4	9.2	16.8	22.4		19.7	12.8	0.0	5.6
srp veins[d]	3.7	5.7	6.4	4.4	7.5		10.8	1.1	6.2	1.0
other srp	4.6	1.9	2.7	0.6	3.9		2.9	0.0	3.5	0.0
mag	0.4	1.0	0.5	0.2	0.4		0.5	1.1	1.3	1.5
vein cab	7.3	0.0	0.0	0.0	0.0		4.0[j]	0.0	2.2[j]	0.0
replacive cab	0.0	0.0	0.0	0.0	0.0		0.0	0.0	0.0	0.0
other minerals[e]	0.0	trace[f]	0.0	trace	0.3		trace	2.5	trace	3.3
degree of alteration[g] [%]	74.1	86.3	88.0	79.3	97.3		69.0	85.9	99.2	79.8
Serpentine polymorphs (with associated phases in brackets)										
mesh rim	lz	lz	lz, (iow)	lz	lz	lz	lz	lz	lz	lz, (iow)
mesh center	lz	lz	lz, (iow)	lz	?[h]	?	-	lz,?	?	lz, (iow, brc)
bastite	lz	lz	lz	lz	lz	-[i]	lz, (tr)[k]	ctl, (tlc)	-	lz
vein	lz, ctl	ctl	ctl, lz	lz, ctl	lz, ctl	ctl	lz, atg	ctl	(brc)	ctl, atg

Locality	Newfoundland PaMa		Iberia PaMa		Guatemala fore-arc		Mariana fore-arc			
Sample no.	S006	S015	S008	S012	S017	S021	S029	S030	S032	S038
Mineral proportions [surface %]										
ol	0.0	0.0	0.0	0.0	0.0	0.3	1.9	2.2	0.6	
opx	0.5	0.0	3.2	0.6	0.0	0.0	0.0	5.1	0.5	
cpx	0.0	0.0	0.4	28.9	0.0	trace	trace	0.6	0.5	
spl	0.2	0.8	0.4	trace	0.3	0.7	0.4	0.4	1.3	
amp	4.7	0.2	trace	0.0	0.0	0.0	0.0	0.0	trace	
mesh rims and centers	51.6	78.0	62.3	7.7	79.0	57.1	87.7	66.0	81.4	
bastite	4.3	1.0	19.6	46.6	12.3	11.6	0.0	7.4	13.4	
srp veins	14.8	3.5	2.8	10.3	6.0	26.1	9.8	7.4	1.0	
other srp	4.5	5.3	8.6	2.6	2.1	4.2	0.0	5.7	0.9	
mag	trace	0.9	0.7	0.4	0.3	0.1	0.3	0.5	0.4	
vein cab	13.3	5.1	1.0	2.0	0.0	0.0	0.0	0.0	0.0	
replacive cab	0.9	3.3	0.0	0.3	0.0	0.0	0.0	0.0	0.0	
other minerals	5.2	1.9	0.9	0.6	trace	trace	trace	4.7	0.0	
degree of alteration [%]	85.3	96.8	94.8	65.6	99.7	98.6	97.5	85.9	97.2	
Serpentine polymorphs (with associated phases in brackets)										
mesh rim	lz	lz	lz	lz	lz	ctl, atg	lz, ctl	ctl	?	lz, ctl
mesh center	?	-	lz	?	lz	?	ctl	ctl	ctl	-
bastite	ctl	lz, ctl	lz	lz,?	lz	ctl, atg	-	lz	lz	lz, (tlc)
vein	ctl	lz,?	lz	lz	ctl	ctl, atg	ctl	(brc)	ctl	lz, (brc)

[a]Estimated by point counting (see Analytical Methods for more information).
[b]Pseudomorphic srp ± brc ± iow after olivine.
[c]srp formed after opx.
[d]Including brc ± mag veins.
[e]tlc, chl, Mn-oxide(s), sulphides, unidentified phases, voids.
[f]Present, but could not be sampled by point counting.
[g]For calculation details see text (Petrography).
[h]srp polymorph could not be determined.
[i]Serpentine not observed in the textural position.
[j]Wide, single vein of cab (separable); percentage has higher uncertainty than in other samples.
[k]tr or tlc indicated in bastite of S025, S033 and S038 occur only along the margins of the bastite pseudomorphs.

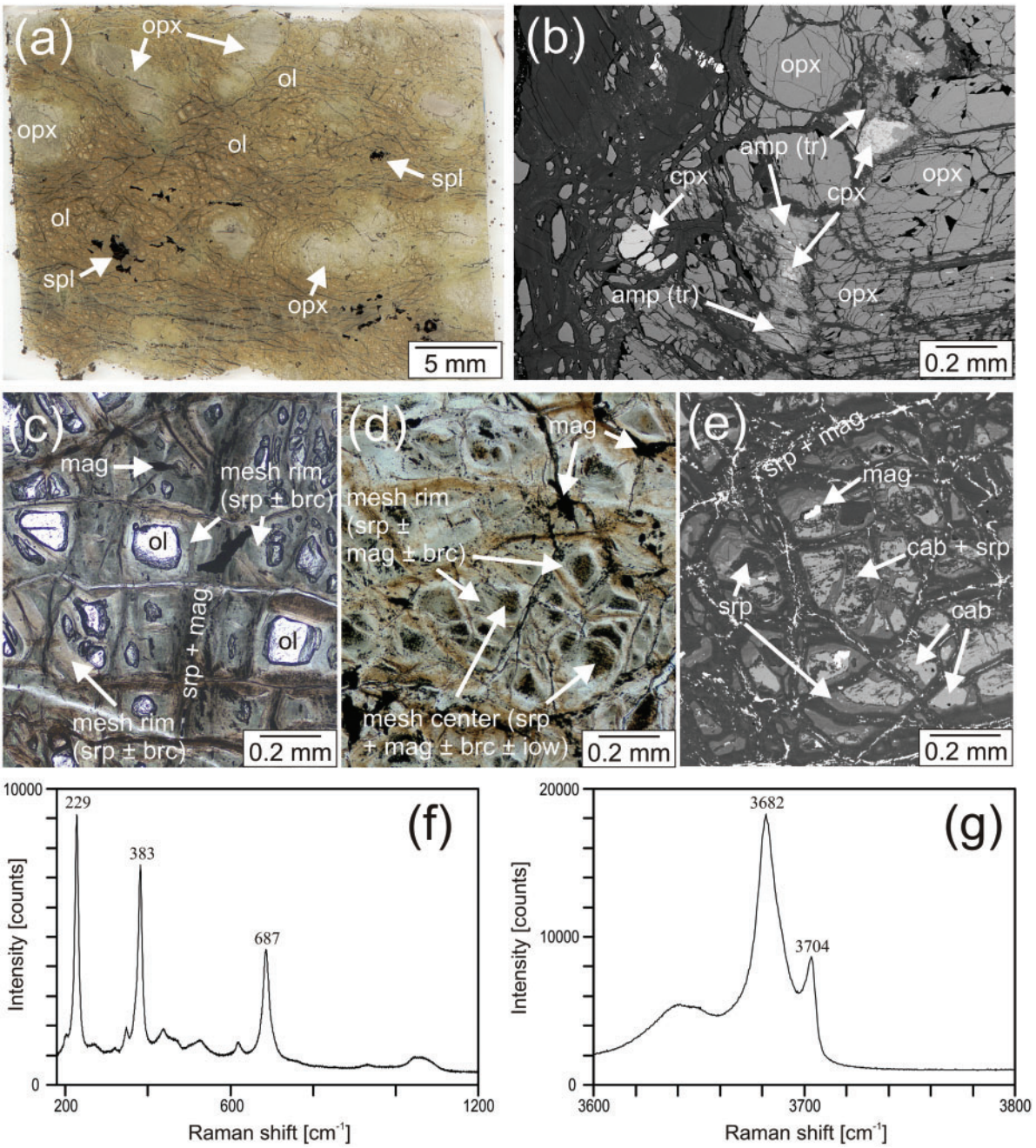

Fig. 1. Relic mantle textures and textures related to the serpentinization of olivine. (a) Undeformed serpentinized peridotite (S039) from the Hess Deep. The original mantle texture can still be recognized (scanned image of a normal petrographic thin section). (b) Hydrothermal tremolite replacing clinopyroxene next to weakly serpentinized orthopyroxene (S039; Hess Deep; BSE image). (c) Pseudomorphic replacement (mesh rims) around relics of olivine. Magnetite is aligned along the mesh network corresponding to relatively high water/rock ratios prevailing between mesh rims (S009; MAR; photomicrograph; plane-polarized light). (d) Mesh rims and centers. Mesh centers sometimes contain Fe-rich brucite. Magnetite is abundant in mesh centers and forms a network around mesh rims (S003; MAR; photomicrograph; plane-polarized light). (e) Mesh centers partially replaced by magnetite and calcite in the totally serpentinized part of S012 serpentinized olivine-websterite (Iberia PaMa; BSE image). (f) The 180–1200 cm^{-1} section of the Raman spectrum of lizardite found in mesh rims (S009; MAR). (g) The 3600–3800 cm^{-1} section of the spectrum displayed in (f). The double, tooth-like peaks at 3682 and 3704 cm^{-1} are typical for lizardite.

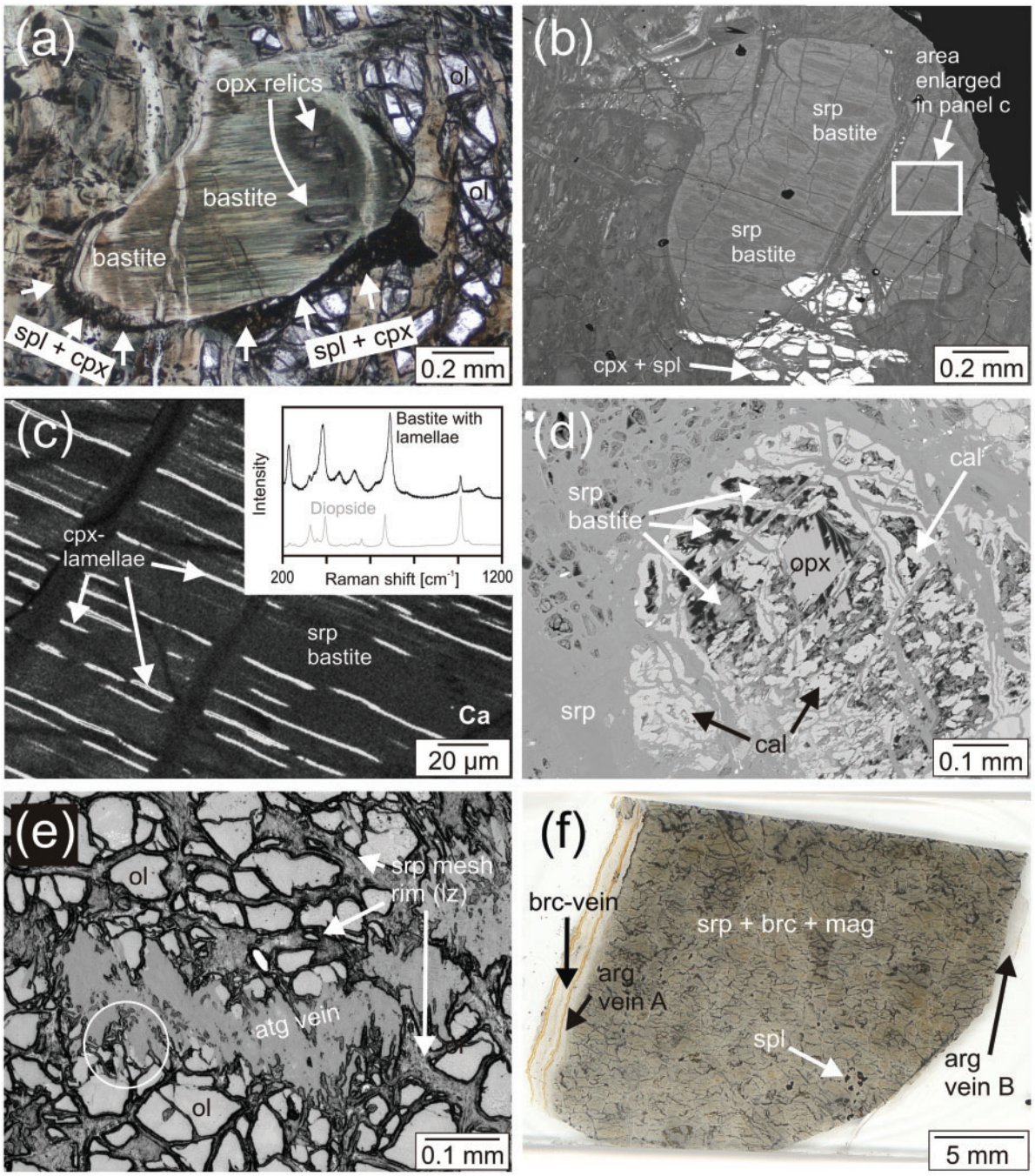

Fig. 2. Textures related to the serpentinization of orthopyroxene and veining. (a) Serpentine bastite. Serpentinization has preserved the original shape of orthopyroxene together with the very fine-grained clinopyroxene + spinel intergrowths along the former grain boundary (S003; MAR; photomicrograph). (b) Bastite and associated relatively unaltered clinopyroxene and spinel (S032; Mariana fore-arc; BSE image). (c) Calcium X-ray map and Raman spectrum of bastite shown in (b), identifying relic clinopyroxene lamellae. (d) Calcite replacement after bastite in S007 (Newfoundland PaMa; BSE image). (e) Antigorite vein in S025 (Hess Deep). Antigorite veins predate pseudomorphic serpentinization, as shown by the direct replacement of olivine by antigorite (circled area; photomicrograph). (f) Widely spaced millimetre-wide veins in S034 serpentinized dunite (Hess Deep). The slightly darker string in the middle of the brucite vein on the left-hand side is a very narrow serpentine vein (scanned image of a normal petrographic thin section). ol, olivine; cpx, clinopyroxene; opx, orthopyroxene; brc, brucite; srp, serpentine.

mineralogy could be determined) may occur around bastite grains or replace them (replacive carbonate, Tables 1 and 3, Fig. 2d) in thoroughly altered samples from the top parts of PaMa core sections.

The hydration of clinopyroxene and the alteration of spinel

Clinopyroxene appears largely unaffected by hydration. Clinopyroxene lamellae within former orthopyroxene can often be traced in bastite grains by Raman spectroscopy and X-ray mapping (Fig. 2c); however, clinopyroxene lamellae are missing in bastite pseudomorphs replaced by carbonate. Replacement of clinopyroxene by tremolite is regarded to be related to seafloor hydration rather than melt–rock interaction (Fig. 1b). Serpentinization of clinopyroxene was not observed in the studied samples.

Alteration of spinel is observed in highly serpentinized samples and manifests itself in chromite-rich alteration rims, which in turn give place to magnetite. Chlorite is often found around altered spinel grains.

Serpentine, brucite and carbonate veins

Serpentine ± magnetite veins, 0·02–5 mm wide and up to several centimetres long, are common in all samples. Serpentine in these veins is mostly chrysotile or lizardite (Table 3). However, veins consisting entirely of antigorite were also observed, in some Hess Deep samples (S025 and S039; Table 3; Fig. 2e). Although antigorite veins are only a subgroup of serpentine ± magnetite veins, they are discussed separately and will be referred to as antigorite veins hereafter.

In few samples (S004, S034, S030 and S038) veins comprising brucite ± magnetite ± serpentine also occur (Fig. 2f). They are 0·01–1·0 mm wide and rarely longer than a couple of millimetres. In Mariana samples they often form a densely packed network with no orientation.

Veins consisting solely of aragonite or calcite are common (12 of the studied 39 samples contain carbonate veins). Carbonate veins were not found in serpentinites sampled deeper than about 40 m below the (paleo-) seafloor (compare Table 1 and Fig. A1 of EA1). Carbonate veins have highly variable dimensions (width 0·01–11 mm; length 5 mm to several centimetres; Fig. 2f). They are structurally late, cutting pseudomorphic serpentine and most serpentine veins. They often form a densely packed (i.e. >3–4 veins per cm^2) network (e.g. S005). However, samples with sparse carbonate veins are also common (e.g. S034; Fig. 2f).

Seafloor weathering

Texturally late features associated with the exhumation-related decomposition of the serpentinite assemblage are here referred to as 'seafloor weathering'. Such features were detected in Newfoundland serpentinites as well as in samples S010 and S014 from the MAR and include the partial dissolution of pseudomorphic serpentine ± brucite together with the precipitation of replacive carbonate (see above; Figs 1e and 2d) and the occurrence of brown Fe-rich oxides and hydroxides as well as Mn-oxides. The Fe-oxides and Mn-oxides form relatively large (about 10–100 times 1–10 μm^2) crystal aggregates. In weathered samples serpentine often has a brownish stain. In some cases this is caused by very small ($d \leq 1$ μm) inclusions of Fe-oxides or hydroxides. In other cases the brownish stain is observable although no metal oxides could be detected.

RESULTS

Bulk-rock major and trace elements

Bulk-rock major and trace element concentrations are listed in EA3. Apart from their high volatile contents (LOI 7·6–22·8 wt %), the studied serpentinites and serpentine muds show refractory major element compositions, typical of upper mantle rocks, with high Mg-numbers (87·6–91·7; Mg-number $= 100 \times [Mg/(Mg + Fe)]_{molar}$, where all Fe is considered Fe^{2+}), and generally low alumina contents (0·14–2·43 wt % except S012 olivine-websterite). Samples with significant carbonate (e.g. S005) have higher CaO and LOI than other serpentinites (EA3).

Overall, the studied serpentinites are depleted in trace elements incompatible during mantle melting, as expected for upper mantle precursors. Many of the incompatible trace elements [especially the high field strength elements (HFSE), such as Th, Nb, Ta and the MREE] are present in extremely low abundances (i.e. ng g^{-1}; EA3).

Notwithstanding this generally depleted nature, serpentinites contain 470–6600 μg g^{-1} Cl and 5·40–170 μg g^{-1} B. The lowest B contents were found in an Iberia PaMa and in a Guatemala fore-arc sample (S016 and S021, respectively). The highest B concentrations were measured in Newfoundland serpentinites. There are only weak correlations between Cl and B concentrations (Fig. 3) and there is no correlation between either of these elements and LOI. We found no correlation between the Cl and B contents of our samples and the depth of sampling or paleo-depth (depth below the interface of basement and sedimentary ± volcanic cover), although such correlations cannot be ruled out, given the small number of samples from single drill holes.

Mid-ocean ridge and fore-arc serpentinites have low REE concentrations and display concave-up chondrite-normalized REE patterns (Fig. 4). Most MOR serpentinites have positive Eu anomalies (Eu_N/Eu_N^* 0·65–5·9, calculated dividing Eu_N by the average of Sm_N and Gd_N, where the N subscript indicates chondrite-normalized concentration of the given element; Fig. 4). PaMa serpentinites and serpentine muds from the Mariana fore-arc show relatively high REE concentrations and convex-upward to flat REE patterns (La_N/Sm_N

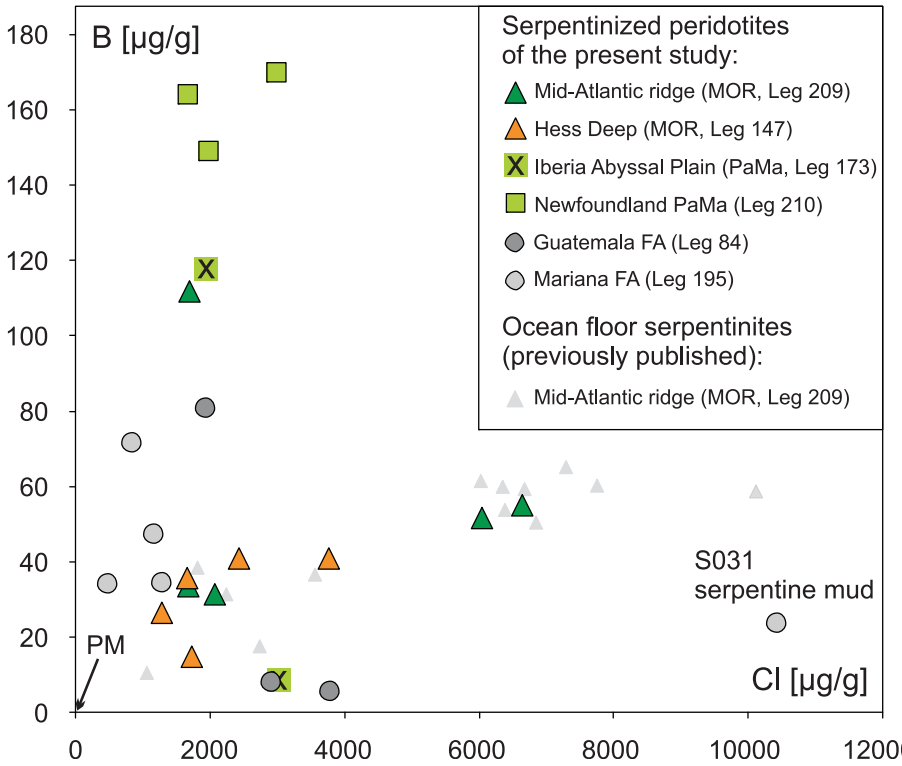

Fig. 3. Variation of Cl and B concentrations in serpentinized peridotites, websterites and serpentine mud. Serpentinized peridotite data previously published by Vils *et al.* (2008) are also indicated. The good agreement between their and our Leg 209 data suggests that using the external parts of the drill cores did not bias the B and Cl measurements [Vils *et al.* (2008) used the inner parts of drill cores for analysis; F. Vils, personal communication]. Black arrow points to the Primitive Mantle (PM; McDonough & Sun, 1995) composition. S031 serpentine mud shows substantially higher amounts of Cl than the other samples, possibly owing to the presence of seawater salt, which could have precipitated from residual porewater after drilling. FA, fore-arc.

0·17–2·39; Gd_N/Lu_N 0·33–2·20; Fig. 4) with relatively small Eu anomalies (Eu_N/Eu_N^* 0·40–1·78; Fig. 4).

Primitive mantle-normalized trace-element variation diagrams for MOR and fore-arc serpentinites display U-shaped patterns (Fig. 5), and mostly show enrichments in U, B, Pb, Sb, Sr and Li relative to elements with similar compatibility during mantle melting (U_N/Th_N 1–16 800; B_N/Nb_N 210–96 000; Pb_N/Ce_N 0·9–280, all but one sample above unity; Sb_N/Ce_N 11–4700; Sr_N/Nd_N 0·85–31 400, again, all but one sample above unity; Li_N/Y_N 2–6100; Fig. 5). Mariana fore-arc and two Guatemala fore-arc serpentinites exhibit strong relative enrichments in large ion lithophile elements (LILE), particularly Cs and Rb (Fig. 5), when compared with other samples. Passive margin serpentinites have generally higher trace element abundances than MOR and most fore-arc serpentinites, and display relatively flat primitive mantle-normalized trace element patterns with positive U, B, Sb, Sr and Li anomalies (Fig. 5).

Major element composition of relic high-temperature minerals

Average major element compositions of olivine, orthopyroxene, clinopyroxene and spinel are listed in EA4 (pp. 1–4). We report average compositions because compositional zoning with respect to major elements is generally negligible in these phases. Only some spinels show compositional zoning. Compositions of zoned spinel grains are given as single analyses (EA4, p. 4).

Olivine major element compositions (EA4, p. 1) are remarkably uniform, characterized by high Mg-number (90·8–92·0) and NiO contents (0·31–0·47 wt %). Orthopyroxene compositions correspond to Al- and Cr-bearing enstatite, with Mg-number (88·8–92·4; EA4, p. 2) similar to that of olivine. All analysed clinopyroxenes are diopside (EA4, p. 3). Average Al_2O_3 contents are highly variable (0·07–7·03 wt %) with the lowest and highest Al_2O_3 concentrations found in the recrystallized lamellae of S038 and in the clinopyroxene of S012 olivine websterite, respectively.

Variations in spinel compositions within samples are often significant but could not be related to textural position in most cases. Zoned spinels show either a continuous transition from Mg- and Al-rich cores towards rims enriched in Fe and Cr (S008; EA4, p. 4), or display an abrupt compositional change from a magnesian spinel core to an Fe-rich chromite rim in extremely hydrated rocks (e.g. S010). Mid-ocean ridge and PaMa

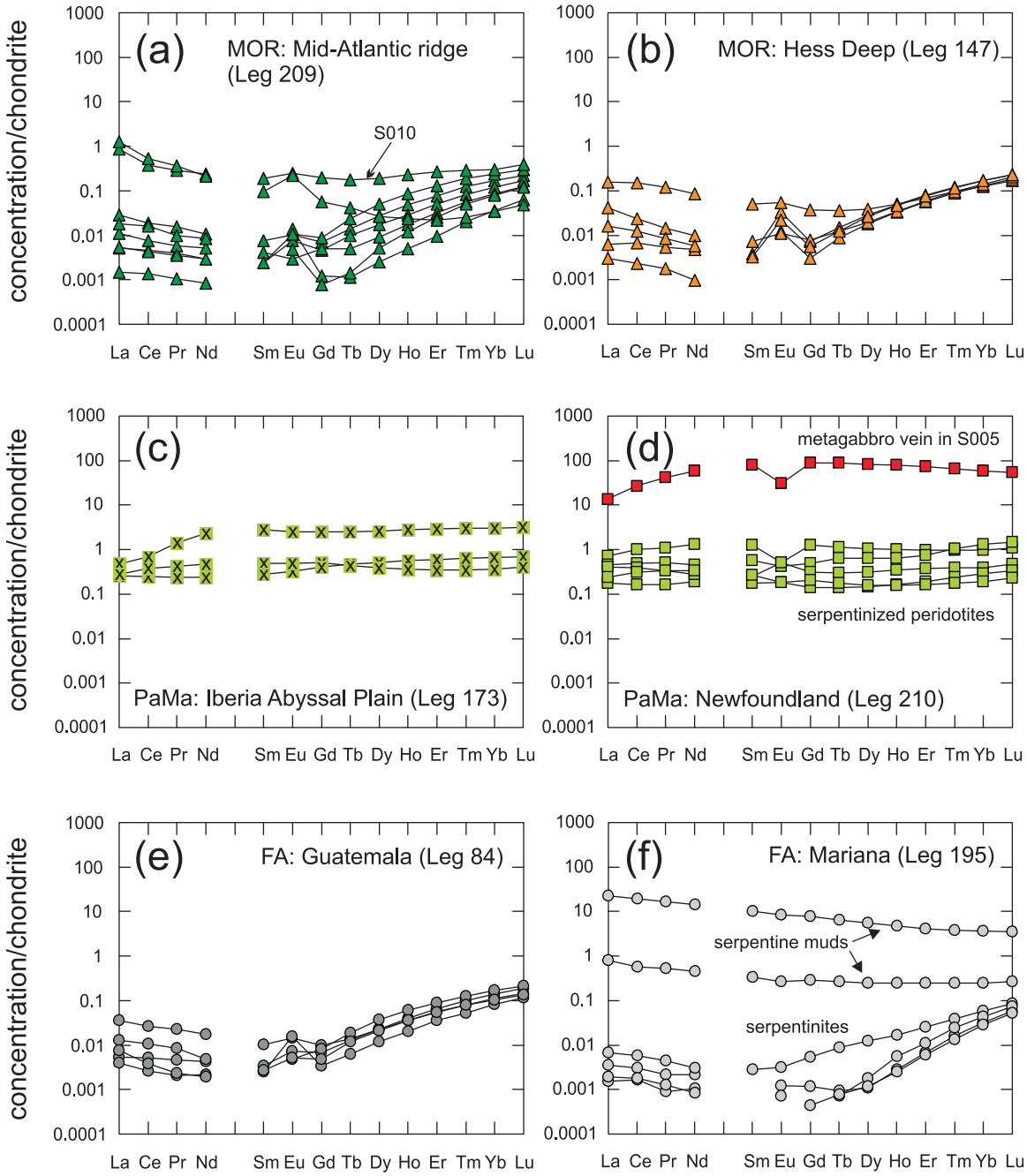

Fig. 4. Chondrite-normalized (McDonough & Sun, 1995) REE concentrations of serpentinized peridotites, websterite, metagabbro and serpentine muds from the (a) Mid-Atlantic Ridge 15°20′N Fracture Zone, (b) Hess Deep, (c) Iberia Abyssal Plain, (d) Newfoundland PaMa, (e) Guatemala fore-arc and (f) Mariana fore-arc, South Chamorro Seamount. The generally U-shaped patterns of MOR and fore-arc serpentinites and the positive Eu anomaly of the MOR and Guatemala samples should be noted. FA, fore-arc.

spinels are generally more magnesian (Mg-number 40·1–70·5) and less chromian (Cr-number 35·8–65·9; Cr-number = $100 \times [Cr/(Cr+Al)]_{molar}$) than fore-arc spinels (Mg-number 31·8–60·6; Cr-number 50·0–68·2). The TiO_2 content of the spinel of MOR, fore-arc and Newfoundland PaMa harzburgites and orthopyroxene-bearing dunites is generally very low (<0·10 wt %), whereas the orthopyroxene-free MOR dunites contain spinel richer in TiO_2 (0·13–0·32 wt %).

Trace element compositions of relic high-temperature silicates

Variations in the trace element contents of relic olivine, orthopyroxene and clinopyroxene within samples,

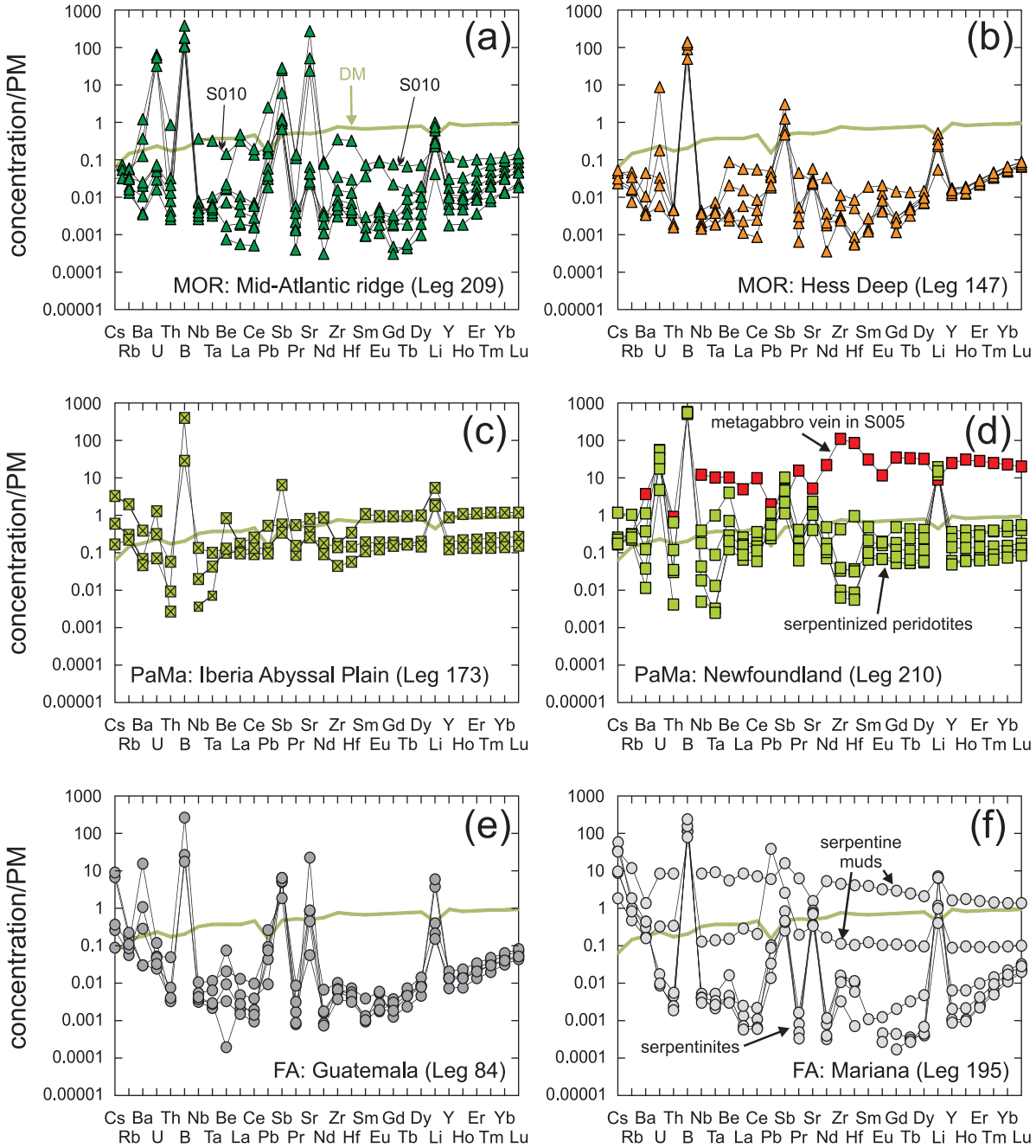

Fig. 5. Primitive mantle (PM) normalized (McDonough & Sun, 1995) trace element concentrations of serpentinized peridotites, websterite, metagabbro and serpentine muds from the (a) Mid-Atlantic Ridge 15°20'N Fracture Zone, (b) Hess Deep, (c) Iberia Abyssal Plain, (d) Newfoundland PaMa, (e) Guatemala fore-arc and (f) Mariana fore-arc, South Chamorro Seamount. Positive anomalies of U, Pb, Sb, Sr, U and Li are observable in all serpentinites but they are missing from the serpentine muds. Depleted mantle (DM) concentrations are from Salters & Stracke (2004). FA, fore-arc.

although sometimes high, could not be linked to textural observations. We therefore report average trace element compositions of these phases (EA4; p. 5), together with standard deviations to provide information on compositional variability. Average element concentrations are often obtained from only a few significant measurements (i.e. where the given element was above LOD) and thus should be considered as maximum average values.

Clinopyroxene shows by far the highest incompatible trace element concentrations among the measured relic

high-temperature silicates, containing 1·6–7·4 μg g^{-1} Li, 1·2–3·8 μg g^{-1} B and 0·18–8·7 μg g^{-1} Sr on average. Sample S001 (MAR) has two types of clinopyroxene with respect to trace element contents. The depleted type (CpxD; EA4) is compositionally similar to the clinopyroxene found in other samples, whereas the enriched type (CpxE) has significantly higher Sr, Ba and LREE contents (Sr^{cpxE} 1·9 μg g^{-1}; Ba^{cpxE} 0·81 μg g^{-1}; Ce^{cpxE} 0·054 μg g^{-1}). The depleted and enriched clinopyroxene grains of S001 were found in the same textural position (equant crystals and spinel–clinopyroxene intergrowths).

Olivine and orthopyroxene are generally characterized by very low incompatible trace element contents. Of the elements incompatible in olivine, only Li, Ti and Cr could be detected routinely (0·89–1·5, 0·50–94 and 13–150 μg g^{-1}, respectively). When above LOD (0·1–0·7 μg g^{-1}; EA4), B is present in sub-μg g^{-1} amounts (0·10–0·28 μg g^{-1}). Sr is below LOD (0·002–0·016 μg g^{-1}) in all but one sample (S030; $Sr^{olivine}$ 0·004 μg g^{-1}). Orthopyroxene contains 0·36–4·1 μg g^{-1} Li on average. Orthopyroxene is generally depleted in Sr (0·01–0·03 μg g^{-1}). Higher Sr contents (0·25 and 0·38 μg g^{-1}) were observed in the orthopyroxene of the Iberia PaMa samples, which also show higher LREE, Y, Zr, and Nb contents than the orthopyroxenes of other localities (e.g. Ce^{opx} 0·02–0·11 μg g^{-1} in Iberia PaMa vs < 0·012 μg g^{-1} in all other orthopyroxenes; EA4).

The few significant B concentrations reported here for relic olivine and orthopyroxene are 1–2 orders of magnitude higher than B contents reported in the literatue for olivine and orthopyroxene in depleted mantle rocks (mostly below 0·04 μg g^{-1}; e.g. Vils *et al.*, 2008), and that estimated for the depleted MORB mantle (0·06 μg g^{-1}; Salters & Stracke, 2004). The high B values were barely reproducible: they represent single measurements in two of the three samples where B was detected in olivine (0·1–0·7 μg g^{-1}; EA4) and in one of the two samples where B was detected in orthopyroxene (0·02–0·9 μg g^{-1}; EA4). It is therefore possible that the few significant B concentrations do not represent true compositions. These data should be regarded as maximum estimates.

Many of our *in situ* Sb measurements (independent of the analysed phase) gave concentrations about one order of magnitude higher than the respective bulk-rock Sb contents (mostly ng g^{-1} level; EA3). Bulk-rock Sb data are likely to be close to true concentration values because our measurement results on the JP-1 peridotite standard are in good agreement with literature data (EA2). Considering the high proportion of serpentine ± brucite in the studied serpentinites (67–99 vol. %; Table 3), the *in situ* serpentine data can hardly represent true Sb abundances, whereas the quality of Sb data for relic olivine, orthopyroxene and clinopyroxene cannot be assessed in the absence of an independent control on pre-serpentinization Sb concentrations. Therefore, Sb abundances reported in EA4 for relic olivine, orthopyroxene and clinopyroxene are to be considered as maximum estimates.

Major element composition of serpentine, brucite, chlorite and hydrothermal amphibole

Major element compositions of serpentine, brucite, iowaite and chlorite are given in EA5 (p. 1). These phases often form intergrowths not resolvable by electron microprobe (see below). Therefore, we list single analyses in EA5 and discuss our data mostly in the context of textural position (rather than mineralogy) in the following sections. Major element compositions of hydrothermal amphiboles are also listed in EA5 (p. 2).

Pseudomorphic serpentine ± brucite ± iowaite

Mesh rims and/or mesh centers of certain samples have compositions between those of serpentine and brucite or iowaite, indicating sub-μm intergrowths of serpentine and hydroxide(s). Accordingly, the silica contents of mesh centers and rims vary considerably (3·36–43·46 wt %, EA5). Analyses with the highest SiO_2 contents are brucite- and iowaite-free. In one sample (S010) the low SiO_2 concentrations in mesh centers are partly due to the presence of carbonate, as indicated by the high CaO concentrations (12·85–36·78 wt %). Mg-numbers (98·0–68·6) decrease with increasing $[(Mg + Fe)/(Si + Al)]_{cation}$ (where all Fe is considered Fe^{2+}; EA5; Fig. 6a and b). This is also indicative of intergrowth with brucite or iowaite, as both minerals are expected to have lower Mg-number than coexisting serpentine and are essentially Si-free (e.g. McCollom & Bach 2009). Cl contents are between 0·02 and 6·60 wt %. The highest Cl abundances, coupled with very low SiO_2 concentrations, may indicate the presence of iowaite (EA5). Mesh centers and rims can contain up to 1·72 wt % Al_2O_3, although the great majority of the analyses have Al_2O_3 below 0·30 wt %. Mesh centers and rims contain up to 0·77 wt % NiO, whereas their Cr_2O_3 content never exceeds 0·24 wt % (Fig. 7).

Bastite contains 33·48–43·42 wt % SiO_2. The Mg-number of bastite varies between 84·7 and 97·8, except for two analyses of the very iron-rich green bastite of S017 (Mg-number 74·4 and 77·8). The strong negative correlation between $[(Mg + Fe)/(Si + Al)]_{cation}$ and Mg-number observed in mesh rims and mesh centers cannot be detected in bastite compositions (Fig. 6a). Bastite has up to 1·05 wt % Cl. The Al_2O_3 concentration in bastite is variable (0·21–10·52 wt %; mostly between 0·50 and 2·00 wt %; EA5). The highest Al_2O_3 concentrations probably represent mixed chlorite–serpentine analyses. Compared with mesh centers and rims, bastite contains less NiO (<0·26 wt %, mostly <0·20 wt %) and more Cr_2O_3 (mostly above 0·40 wt % up to 1·32 wt %; Fig. 7).

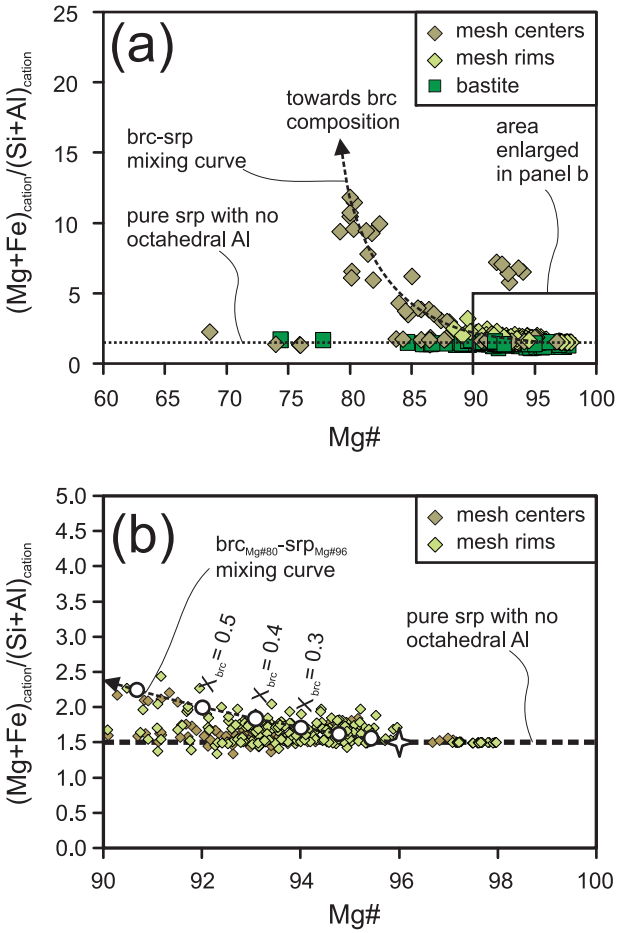

Fig. 6. Plot of $[(Mg + Fe)/(Si + Al)]_{cation}$ vs Mg-number of pseudomorphic serpentine ± brucite. (a) The entire compositional range found in the studied serpentinites. Mesh center and rim compositions lie close to the mixing curve between serpentine, $[(Mg + Fe)/(Si + Al)]_{cation} \sim 1{\cdot}5$, Mg-number > ~ 90, and brucite $[(Mg + Fe)/(Si + Al]_{cation} \gg 25$, Mg-number ~ 80. (b) The compositional range corresponding to Mg-number between 90 and 100 and $[(Mg + Fe)/(Si + Al)]_{cation}$ of 0–5. For the sake of clarity, bastite compositions are omitted. Assuming Mg-number = 80 brucite as one end-member and Al-free, Mg-number = 96 serpentine as another (white star, chosen as an end-member composition because the vast majority of analyses have lower Mg-number), we estimated the amount of brucite in the mixed analyses (white dots with the molar fraction of brucite, X_{brc}, in the mixture). All iron is regarded as Fe^{2+}. This calculation maximizes brucite contents, which in reality are probably lower.

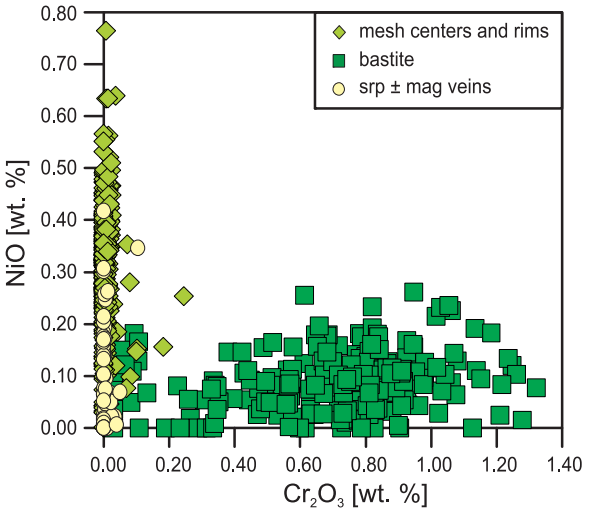

Fig. 7. NiO vs Cr_2O_3 contents (wt %) of pseudomorphic serpentine ± brucite and serpentine ± magnetite veins. Pseudomorphic replacements after olivine (mesh centers and rims) and orthopyroxene (bastite) are easily distinguishable, suggesting limited mobility of Ni and Cr during serpentinization.

Serpentine and brucite of veins

Analyses of serpentine ± magnetite veins suggest that serpentine–brucite mixtures are also present in this vein type. Si contents vary between 33·81 and 42·83 wt %, and Mg-numbers are between 88·1 and 98·6. Cl concentrations are between 0·02 and 1·11 wt %. Serpentine of this vein type contains up to 3·40 wt % Al_2O_3 (mostly <2·00 wt %), less than 0·10 wt % Cr_2O_3 and less than 0·42 wt % NiO (mostly below 0·30 wt % (EA5).

Brucite of brucite ± magnetite ± serpentine veins (EA5) has higher Mg-number (88·8–94·5) than the values inferred from mixed serpentine–brucite analyses of mesh centers and rims (EA5). Cl and Al_2O_3 contents remain below 0·16 and 0·03 wt %, respectively. Cr_2O_3 was detected only once (0·01 wt %).

Chlorite and amphibole

Chlorite compositions correspond to clinochlore with 11·32–16·56 wt % Al_2O_3, and Mg-numbers between 88·1 and 97·5 (EA5). Chlorite occurring as alteration product after spinel contains significantly more Cr_2O_3 (3·09–3·30 wt %) than chlorite in other textural positions (Cr_2O_3 < 1·23 wt %; EA5).

Amphibole found as replacement after clinopyroxene (Fig. 1b) is mainly tremolite with variable Al_2O_3 (0·96–5·10 wt %; EA5), relatively high Cr_2O_3 (0·34–1·13 wt %) and low TiO_2 (<0·08 wt %). Anthophyllite found on the margins of a serpentine vein of S006 has considerable ferro-anthophyllite component: Mg-numbers are between 88·8 and 89·4. Alumina contents are low (0·21–0·41 wt % Al_2O_3; EA5).

Trace element composition of serpentine ± brucite pseudomorphs, serpentine ± magnetite veins and hydrothermal amphibole

Trace element compositions of serpentine ± brucite pseudomorphs and (hydrothermal) tremolite in S039 (Hess Deep) are presented in EA5 (p. 3 and p. 4, respectively). LA-ICP-MS measurements on serpentine ± brucite (but not on other phases) often yielded ^{208}Pb signals which decreased relative to the signals of other isotopes during ablation. As shown in Fig. A2 (EA6), the ratio of,

for example, ^{11}B and ^{88}Sr signal intensities over that of the internal standard isotope ^{25}Mg do not change significantly during ablation, whereas the signal intensity ratios normalized to ^{208}Pb increase by one order of magnitude. These ^{208}Pb signals do not correlate with other isotope signals. Lead concentrations calculated from such signals are up to 20 times higher than bulk-rock concentrations. Together, these observations suggest that Pb measurements on serpentine are biased, possibly by contamination introduced during thin section polishing. Therefore, we do not report Pb concentration data for serpentine ± brucite.

Most of our *in situ* Sb measurements on serpentine ± brucite gave concentrations about one order of magnitude higher than the respective bulk-rock Sb contents (as noted for relic high-temperature silicates above), although without the peculiar signal shape shown by Pb. We suspect that these measurements are biased by instrumental memory effects. Serpentine Sb data considered to be biased are highlighted in EA5. We did not detect instrumental memory effects for analytes other than Sb. This is confirmed by the good agreement between the *in situ* serpentine ± brucite and bulk-rock trace element data (for carbonate-free samples).

Pseudomorphic serpentine ± brucite

The most abundant lithophile trace elements in serpentine ± brucite pseudomorphs are B and Sr. Both elements show large variations in their concentrations within and between samples (3·2–280 $\mu g\,g^{-1}$ and 0·13–34 $\mu g\,g^{-1}$, respectively; EA5; Fig. 8a–f). Pseudomorphic serpentine ± brucite in the PaMa serpentinites contains more B on average (150 $\mu g\,g^{-1}$) than serpentine from other settings (70 $\mu g\,g^{-1}$), in line with our bulk-rock data (EA3). In MOR and Mariana fore-arc samples mesh centers and rims contain significantly less B than bastite ($B^{\text{mesh centers and rims}}$ 6·0–140 $\mu g\,g^{-1}$, average 48 $\mu g\,g^{-1}$; B^{bastite} 46–180 $\mu g\,g^{-1}$, average 98 $\mu g\,g^{-1}$; Fig. 8a, b and f). B concentrations in mesh centers, rims and bastite of single Iberia PaMa and Guatemala fore-arc samples are in about the same range (e.g. S017, $B^{\text{mesh centers and rims}}$ 36–140 $\mu g\,g^{-1}$; B^{bastite} 23–150 $\mu g\,g^{-1}$), whereas bastite in the Newfoundland PaMa samples has either much lower (S015; $B^{\text{mesh centers and rims}}$ 150–170 $\mu g\,g^{-1}$; B^{bastite} 15–67 $\mu g\,g^{-1}$) or slightly higher (S006; $B^{\text{mesh centers and rims}}$ 130–240 $\mu g\,g^{-1}$; B^{bastite} 220–250 $\mu g\,g^{-1}$) B concentrations than mesh pseudomorphs. Sr concentrations in pseudomorphic serpentine ± brucite of fore-arc and PaMa samples (0·61–34 $\mu g\,g^{-1}$) are significantly higher than in MOR serpentinites (0·13–3·46 $\mu g\,g^{-1}$). Among all the studied samples, the Mariana fore-arc serpentinites contain the most Sr-rich serpentine (1·71–34 $\mu g\,g^{-1}$; EA5; Fig. 8f). Sr concentrations in bastite are always higher than in mesh centers and rims. The difference between the Sr contents of bastite and mesh serpentine is smaller in PaMa (average $Sr^{\text{mesh centers and rims}}$ 3·8 $\mu g\,g^{-1}$; average Sr^{bastite} 5·3 $\mu g\,g^{-1}$) than in MOR (average $Sr^{\text{mesh centers and rims}}$ 0·44 $\mu g\,g^{-1}$g; average Sr^{bastite} 1·5 $\mu g\,g^{-1}$) and in all but one (S021) of the fore-arc serpentinites (average $Sr^{\text{mesh centers and rims}}$ 5·8 $\mu g\,g^{-1}$; average Sr^{bastite} 13 $\mu g\,g^{-1}$).

Li concentrations in mesh centers and rims are between 0·03 and 4·9 $\mu g\,g^{-1}$, except for the Newfoundland PaMa samples (S006 and S015) and one sample from the Mariana fore-arc (S030), which have significantly higher Li contents (14–33 $\mu g\,g^{-1}$). Bastite has a very wide range of Li contents (0·14–180 $\mu g\,g^{-1}$). Resembling the trend observed for mesh rims, bastite pseudomorphs in S006, S015 and S030 have the highest Li concentrations (8·3–180 $\mu g\,g^{-1}$).

Rb and Cs have very variable but generally low concentrations (mostly <1 $\mu g\,g^{-1}$) in serpentine ± brucite pseudomorphs (EA5). Serpentine ± brucite pseudomorphs of Mariana fore-arc serpentinites have higher Rb and Cs contents (Rb 0·04–1·3 $\mu g\,g^{-1}$; Cs 0·016–1·4 $\mu g\,g^{-1}$) than those of MOR and PaMa samples (Rb 0·005–0·74 $\mu g\,g^{-1}$; Cs 0·003–0·03 $\mu g\,g^{-1}$). Guatemala fore-arc samples analysed *in situ* (S017 and S021) show highly variable Rb concentrations in pseudomorphic serpentine ± brucite (0·02–2·6 $\mu g\,g^{-1}$; EA5). Where detected, Rb and Cs are usually more abundant in bastite than in mesh centers and rims. Differences in the Rb and Cs contents of pseudomorphic serpentine ± brucite of single samples are higher for fore-arc than for MOR and PaMa serpentinites.

Pseudomorphic serpentine ± brucite contains LREE to MREE often below the detection limit of LA-ICP-MS (EA5). Generally, chondrite-normalized serpentine ± brucite REE patterns resemble those of the respective bulk-rock (Fig. 9a–c). However, the bastite of S003 (MAR) shows a relatively continuous increase in chondrite-normalized REE from La to Lu with no Eu anomaly, significantly differing from the sample's U-shaped bulk-rock pattern with a positive Eu anomaly (Fig. 9a).

The concentration of U in pseudomorphic serpentine ± brucite is usually below the detection limit (0·001–0·010 $\mu g\,g^{-1}$). Where detected, U has variable concentrations (0·001–3·25 $\mu g\,g^{-1}$; EA5). There is no systematic variation between the U content of mesh centers, rims or bastite within samples.

Serpentine and brucite of veins

Similar to pseudomorphic serpentine ± brucite, the most abundant trace elements in the serpentine ± magnetite veins are B (7·8–230 $\mu g\,g^{-1}$) and Sr (0·23–17 $\mu g\,g^{-1}$), although Li and As concentrations can also be high (0·15–38 and 0·061–0·426 $\mu g\,g^{-1}$, respectively; EA5). The analysed antigorite veins (S025, Hess Deep) have lower B and Sr contents (2·5–3·6 and 0·05–0·07 $\mu g\,g^{-1}$, respectively) than the lizardite or chrysotile veins. A pure brucite vein (S034) contains only 0·33–0·56 $\mu g\,g^{-1}$ B, whereas Sr was not detectable (EA5).

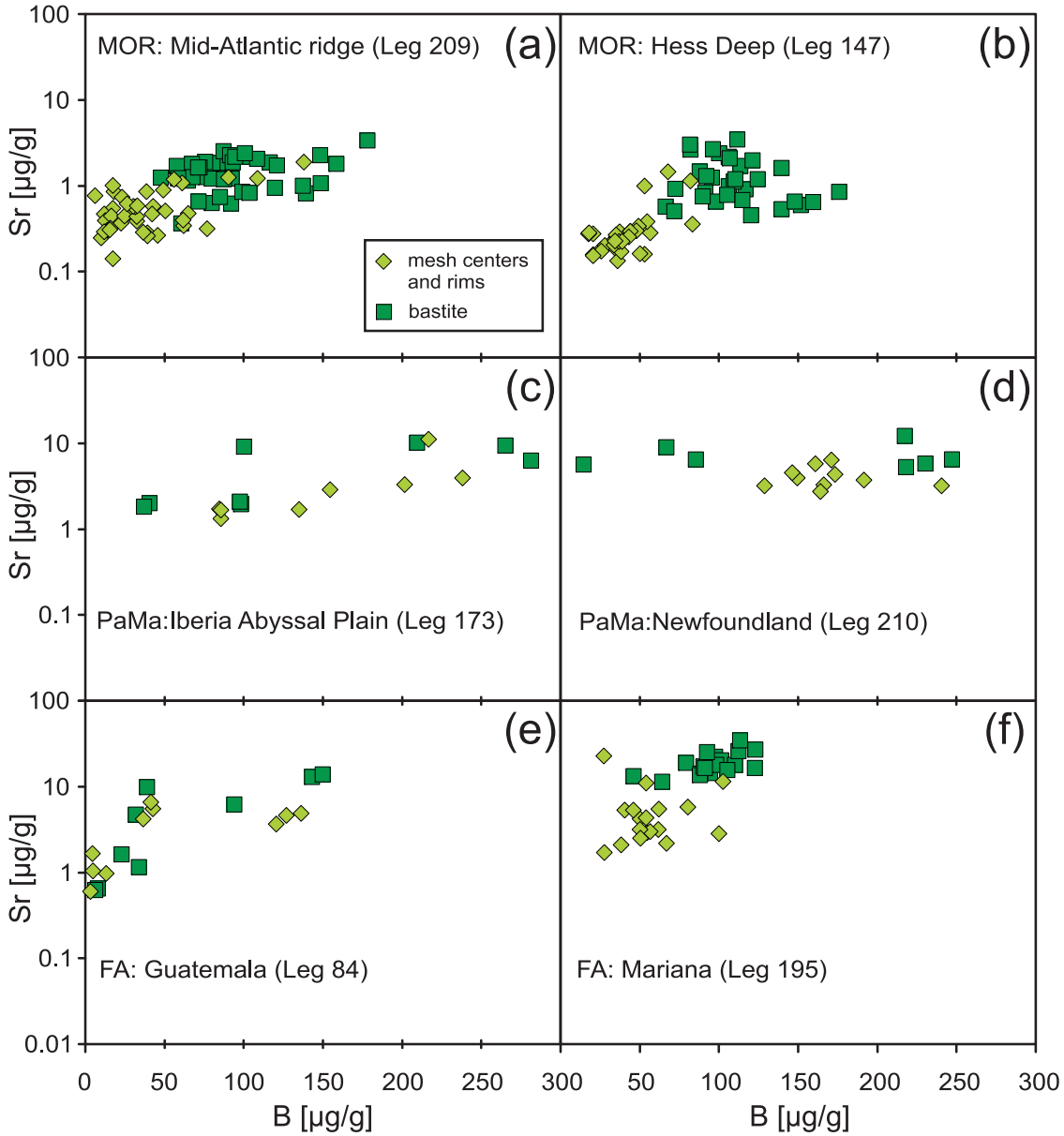

Fig. 8. B and Sr concentrations in pseudomorphic serpentine ± brucite from the (a) Mid-Atlantic Ridge 15°20'N Fracture Zone, (b) Hess Deep, (c) Iberia Abyssal Plain, (d) Newfoundland PaMa, (e) Guatemala fore-arc and (f) Mariana fore-arc, South Chamorro Seamount. Bastite in MOR and Mariana fore-arc serpentinites has considerably more B and Sr than mesh centers and rims from the same localities. The high Sr contents in Mariana fore-arc serpentine ± brucite pseudomorphs relative to the Sr content of serpentine ± brucite from MOR should also be noted. FA, fore-arc.

Serpentine ± magnetite veins have variably low Rb and Cs concentrations (0·02–0·43 µg g^{-1} and 0·001–0·02 µg g^{-1}, respectively (EA5). Rb and Cs contents of antigorite veins are below the detection limit. The brucite vein of S034 did not give an Rb signal and was not analysed for Cs.

Where detected, LREE concentrations in serpentine ± magnetite veins (e.g. Ce 0·003–0·32 µg g^{-1}) are generally higher than the LREE content of most replacements. In contrast, the HREE contents are mostly lower (e.g. Yb 0·008–0·016 µg g^{-1}) than observed for pseudomorphic serpentine (EA5). The REE abundances in the antigorite veins (S025) and in the brucite vein (S034) are below the detection limit (0·006–0·014 µg g^{-1}; EA5) in almost all cases.

Most serpentine ± magnetite veins contain little uranium (U < 0·043 µg g^{-1}; EA5). Only S006, S015 (Newfoundland PaMa) and S025 (Hess Deep) have elevated U contents in their serpentine ± magnetite veins

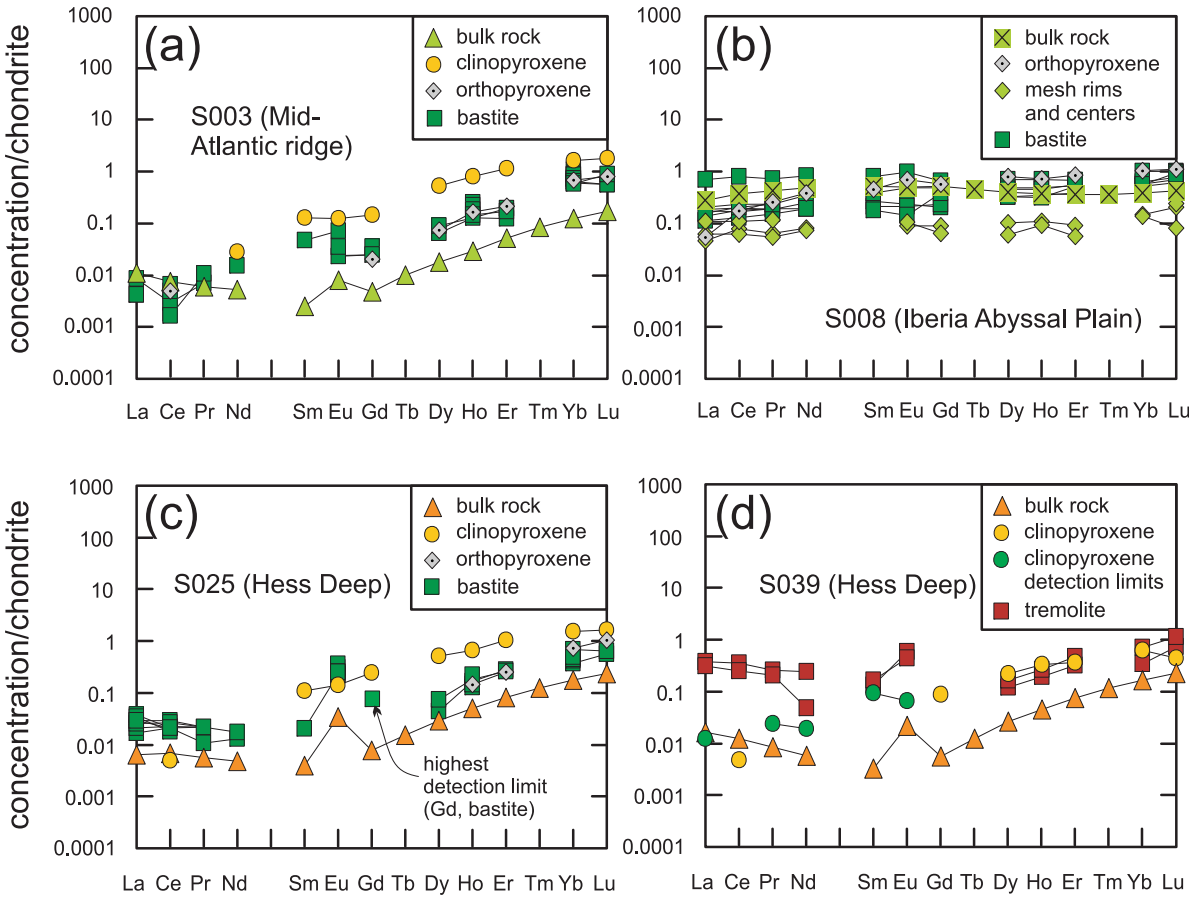

Fig. 9. Chondrite-normalized (McDonough & Sun, 1995) REE patterns of relic mantle phases and their hydrothermal replacements in selected serpentinites together with corresponding bulk-rock data. (a) Barely noticeable Eu anomaly and LREE enrichment in the bastite of S003 (MAR) relative to that of orthopyroxene. (b) LREE enrichment relative to precursor orthopyroxene is noticeable in the bastite of S008 (Iberia PaMa). It should be noted that mesh centers and rims have the same REE distribution as bastite. (c) Relative LREE enrichment and positive Eu anomaly in S025 (Hess Deep) bastite matching the bulk-rock pattern. Although the LREE contents of orthopyroxene were below the detection limit, partitioning behaviour of LREE between clinopyroxene and orthopyroxene [$D^{cpx/opx}$ (LREE) > 20 at 1·5 GPa and T > 1200°C; Witt-Eickschen & O'Neill, 2005] suggests that the observed bastite LREE abundances are elevated relative to the precursor. (d) Hydrothermal tremolite in S039 (Hess Deep) displaying relative LREE enrichment and positive Eu anomaly, similar to the bulk-rock pattern. Whereas tremolite has almost identical HREE contents to those of clinopyroxene, the Ce concentration and the limit of detection of clinopyroxene analyses suggest that LREE abundances have increased through hydration.

(0·14–0·20 μg g^{-1}, 0·38–0·45 μg g^{-1} and 0·03–0·29 μg g^{-1}, respectively). Antigorite veins in S025 have U contents between 0·12 and 0·18 μg g^{-1}. U was barely detectable in the brucite vein of S034 (0·001 μg g^{-1}).

Hydrothermal amphibole

Li and B contents of the tremolite replacing clinopyroxene (Fig. 1b) are 0·32–0·41 μg g^{-1} and 6·8–7·1 μg g^{-1}, respectively (EA5). Sr concentrations in tremolite (3·1 and 3·2 μg g^{-1}) are significantly higher than the Sr content of the replaced clinopyroxene (0·45 μg g^{-1}; EA4), whereas Nb contents are comparable in the two minerals (0·02 μg g^{-1}; EA4 and 5), consistent with a hydrothermal origin of the tremolite. Chondrite-normalized REE concentrations (e.g. Ce_N 0·25–0·36; Sm_N 0·13–0·17; Eu_N 0·44–0·58; Lu_N 0·73–1·13; EA5) show a relatively flat, slightly U-shaped pattern and display a positive Eu anomaly, similar to that of the bulk-rock (Fig. 9d).

Trace element composition of carbonates

Calcite and aragonite have trace to minor Mg, Sr, Mn, Fe and Na contents (EA5, p. 5). Aragonite commonly has higher trace element abundances than calcite (e.g. 14 100 vs 430 μg g^{-1} Sr, 49 vs 3·2 μg g^{-1} B; maximum values). The REE show the opposite trend, displaying higher concentrations in calcite than in aragonite (e.g. 7·9 vs 0·03 μg g^{-1} Ce, 0·70 vs 0·02 μg g^{-1} Eu and 0·09 vs < 0·009 μg g^{-1} Lu; maximum values). Generally, aragonite has higher U (0·008–4·45 μg g^{-1}) contents than calcite (0·003–0·017 μg g^{-1}). Carbonate replacing bastite in S015 could

not be identified as calcite or aragonite, but shows trace element concentrations similar to those of calcite, except for the very low REE concentrations.

DISCUSSION

Pre-serpentinization magmatic and metamorphic history

Refractory mineralogy and depleted chemical character of precursor peridotites

Most of the studied rocks had a refractory mineralogy prior to serpentinization (dominated by olivine and orthopyroxene) with only minor clinopyroxene (0–4% in all but one sample) and spinel (Tables 2 and 3). Petrographic observations indicate that clinopyroxene remained largely unaffected by hydration (Fig. 2c), implying that the low abundance of clinopyroxene observed in most of the studied rocks is a pre-serpentinization feature. This suggests that most of the precursor peridotites had undergone almost complete clinopyroxene exhaustion through partial melting or represent clinopyroxene-free cumulates.

In accordance with these observations, all rocks have high Mg-number (87·6–91·7), indicating a refractory nature regardless of their origin (e.g. melting residues, cumulates). Bulk-rock MgO/SiO_2 and Al_2O_3/SiO_2 ratios plot at the refractory end of the melting trend defined by MOR and fore-arc peridotites studied previously (Fig. 10), which indicates that the protoliths had experienced considerable melting, as serpentinization has little effect on the Al_2O_3/SiO_2 ratios of peridotites (Snow & Dick, 1995; Paulick *et al.*, 2006). Rare deviations from the melting trend can be linked to pre-serpentinization lithological differences (e.g. S012 olivine-websterite, S034 dunite) or seafloor weathering (e.g. S014; see Snow & Dick, 1995).

The major and trace element contents of relic high-temperature phases also indicate the refractory and depleted chemical character of most of the precursor lithologies (EA4). Mg-numbers of olivine and orthopyroxene (90·8–92·0 and 88·8–92·4, respectively) are higher than those estimated for the depleted mantle (89·4; Salters & Stracke, 2004). Trace element concentrations in olivine, orthopyroxene and clinopyroxene (EA4) are generally lower than depleted mantle values (Salters & Stracke, 2004).

Spinel Cr-numbers indicate a high degree (14–20%) of partial melt extraction (EA4; Hellebrand *et al.*, 2001). The Guatemala and Mariana fore-arc peridotites show the highest degrees of melt removal (17–20%), whereas the lowest degree of melting was estimated for the PaMa peridotites (14–18%). It should be noted, however, that no primary clinopyroxene was identified in samples

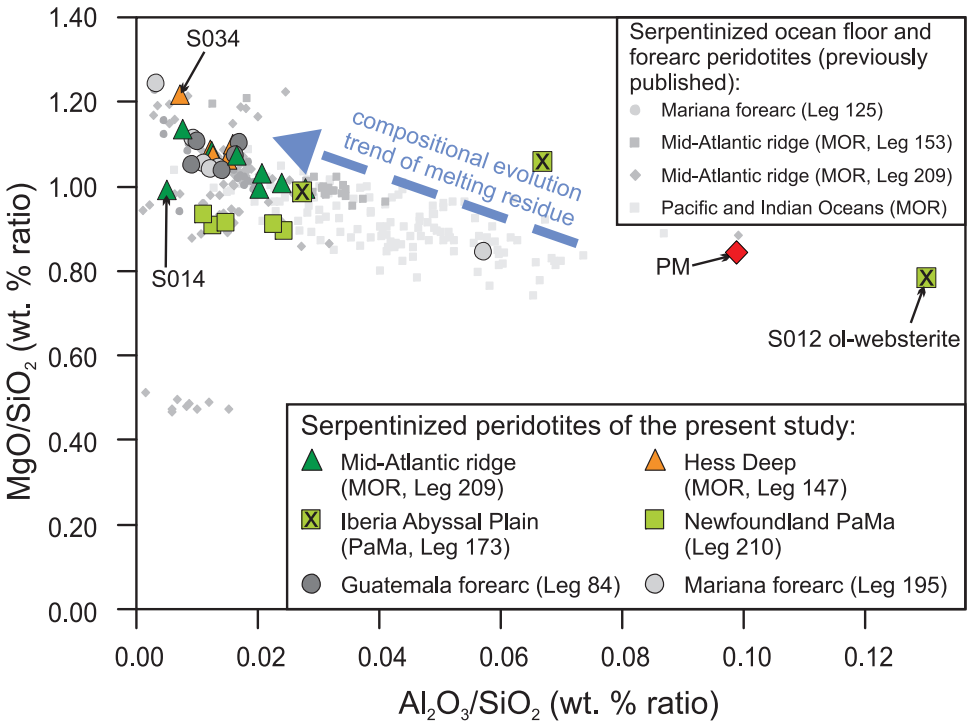

Fig. 10. Al_2O_3/SiO_2 vs MgO/SiO_2 (wt % ratios) of serpentinized peridotites, olivine-websterite and serpentine muds. Previously published data are from Parkinson & Pearce (1998; ODP Leg 125), Stephens (1997; ODP Leg 153), Paulick *et al.* (2006; ODP Leg 209) and Niu (2004; Pacific and Indian Ocean). Primitive mantle (PM) composition is from McDonough & Sun (1995). (See text for details.)

S006, S007, S015 (Newfoundland PaMa) as well as S017 and S021 (Guatemala fore-arc), which may bias the estimations towards higher melting degrees (Hellebrand *et al.*, 2001).

Refertilization and trace element enrichment by melt–rock reaction in mid-ocean ridge peridotites

Channelized melt flow prior to serpentinization can lead to significant incompatible trace element (e.g. LREE) enrichments in serpentinite precursors, although this type of enrichment can be distinguished from that introduced by serpentinization (see below) because it increases HFSE concentrations (e.g. Paulick *et al.*, 2006). This can be traced in at least one of the metadunites (S010; Figs 4 and 5). Based on its pre-serpentinization mineralogy (olivine + spinel) and Ti-rich spinel compositions (EA4) S010 either was a dunite cumulate or represents a reaction zone between mantle and a MORB-type melt (e.g. Arai & Matsukage, 1996; Dick & Natland, 1996; Müntener *et al.*, 2004). The ultrabasic major element composition of S010 dunite combined with its relatively high trace element (especially HFSE) abundances [e.g. Th is 0·86 times Primitive Mantle (PM) in S010 compared with 0·003–0·03 times PM in other samples from the same locality] and flat chondrite-normalized REE pattern (Fig. 4a), however, is best explained by reaction between refractory upper mantle rocks and a percolating, trace element-rich melt. (The trace elements could be hosted originally by minor plagioclase or trace element-rich accessory phases, which may have been totally destroyed by hydrothermal alteration.)

Crystallization of clinopyroxene owing to pervasive melt infiltration is likely to have occurred in many of our MAR peridotites (e.g. S001, S003 and S009), as evidenced by clinopyroxene or complex spinel–clinopyroxene intergrowths around the rounded margins of what used to be orthopyroxene (Fig. 2a; see Seyler *et al.*, 2007). These textures can be interpreted as products of orthopyroxene dissolution with coeval clinopyroxene ± spinel ± olivine precipitation, a reaction expected to occur when MORB-type melts produced at depth migrate through shallower mantle rocks (Jaques & Green, 1980; Falloon *et al.*, 1988). Precipitation of clinopyroxene may increase bulk-rock trace element concentrations (e.g. Sano & Kimura, 2007). However, all analysed textural types of clinopyroxene found in MOR samples have similarly low trace element abundances (EA4). Significant but non-systematic (i.e. with respect to textural type) trace element variability was observed only in sample S001 (cpxD and cpxE; EA4). Therefore, pervasive melt infiltration that produced interstitial clinopyroxene appears not to have significantly enriched the bulk-rock trace element inventory of the studied MAR peridotites.

Primitive mantle-like trace element composition of passive margin peridotites

Samples from the Iberia and Newfoundland PaMa display the highest overall incompatible trace element contents (EA3; Fig. 5) with relatively flat chondrite-normalized REE and PM-normalized trace element patterns (Figs 4c, d and 5c, d). The overall trace element patterns are primarily a pre-serpentinization feature at both localities.

Thoroughly altered (former) gabbro veins, which are sometimes not separable from the bulk serpentinites, and microscopic trails of high-Al amphibole, are frequently observed in the Newfoundland PaMa serpentinized peridotites, indicating infiltration by a (presumably) basaltic melt. Bulk-rock analysis of one of the gabbro veins (metagabbro vein in S005; EA3) suggests that these veins can be enriched in trace elements (up to 100 times relative to PM and 100–1000 times relative to the host peridotite; Fig. 5d). Gabbro veins could thus significantly contribute to the trace element inventory of peridotites from this locality prior to serpentinization.

However, *in situ* trace element analysis of orthopyroxene and bastite in Leg 210 serpentinites shows that the abundances of Li, B, Sr and U also increased significantly during serpentinization (e.g. $Sr^{opxS006} < 0{\cdot}016\ \mu g\ g^{-1}$, $Sr^{bastiteS006}$ 5·3–12 $\mu g\ g^{-1}$; EA4 and 5). None the less, the alteration of gabbro veins during serpentinization could provide some of the trace elements found in elevated concentrations in serpentine ± brucite pseudomorphs in these samples.

Iberian PaMa serpentinites also exhibit evidence for pre-serpentinization trace element enrichment, which could be caused by metasomatism by melt(s) with high incompatible trace element concentrations relative to the depleted upper mantle. Orthopyroxene of S008 serpentinized harzburgite is significantly richer in incompatible trace elements (e.g. Sr 0·38 $\mu g\ g^{-1}$; Y 1·2 $\mu g\ g^{-1}$; Zr 3·1 $\mu g\ g^{-1}$) than orthopyroxene in MOR and fore-arc samples (Sr 0·01–0·03 $\mu g\ g^{-1}$; Y 0·01–0·31 $\mu g\ g^{-1}$; Zr 0·01–0·02 $\mu g\ g^{-1}$; EA4) while having similarly refractory major element compositions (e.g. Mg-number 91·9–92·0 for S008 orthopyroxene vs 91·1–92·4 for MOR and fore-arc orthopyroxenes). This indicates a multi-stage evolution with partial melting followed by enrichment through melt–rock interaction. Although the orthopyroxene and clinopyroxene of S012 have slightly lower Mg-number and Cr_2O_3 contents than those of S008 orthopyroxene and clinopyroxene, they also display elevated trace element concentrations (e.g. $Sr^{opx,S012}$ 0·25 $\mu g\ g^{-1}$; $Zr^{opx,S012}$ 0·76 $\mu g\ g^{-1}$; $Sr^{cpx,S012}$ 8·8 $\mu g\ g^{-1}$; $Zr^{cpx,S012}$ 3·9 $\mu g\ g^{-1}$; EA4). Our data thus document that the Iberia PaMa peridotites had higher overall incompatible trace element contents prior to serpentinization than MOR and fore-arc peridotites, owing to magmatic processes (i.e. melt–rock reaction

and/or cumulate formation), consistent with previous studies (e.g. Seifert & Brunotte, 1996; Hébert *et al.*, 2001).

Relative Li enrichment prior to serpentinization

Primitive mantle-normalized bulk-rock Li concentrations in serpentinites are significantly higher than those of other elements showing similar compatibility during mantle melting (e.g. Li_N/Y_N: 1·9–6l00; Fig. 5a–f). Relic mantle silicate minerals commonly show relative Li enrichment [Li_N/Y_N(ol) 380–830; Li_N/Y_N(opx) 2·5–520; Li_N/Y_N(cpx) 0·56–490; EA4] and spinel can hardly compensate for the high Li_N/Y_N exerted by these silicates owing to its low abundance (Table 3) and trace element-poor chemistry, even if it had $Li_N/Y_N < 1$ (which is unlikely based on existing data; Seitz & Woodland, 2000; Witt-Eickschen & O'Neill, 2005). Furthermore, the Li contents of mesh centers and rims of MOR and most fore-arc serpentinites are lower than those found in the olivine replaced (EA4 and EA5), in line with previous findings (Vils *et al.*, 2008). However, bastite pseudomorphs in the same samples display higher Li concentrations than measured in the replaced orthopyroxene (EA4 and 5).

Together, these observations demonstrate that bulk-rock Li enrichments relative to elements of similar compatibility are a pre-serpentinization mantle feature that can be further enhanced or suppressed by serpentinization. Primary Li enrichment could be caused by, for example, melt–rock interaction if the metasomatizing melts had high Li_N/REE_N and/or they could not equilibrate with the rock-forming phases. In the latter case kinetic effects (i.e. the faster diffusion of Li relative to MREE–HREE; e.g. Cherniak, 2010; Dohmen *et al.*, 2010) could dominate the Li vs MREE–HREE distribution.

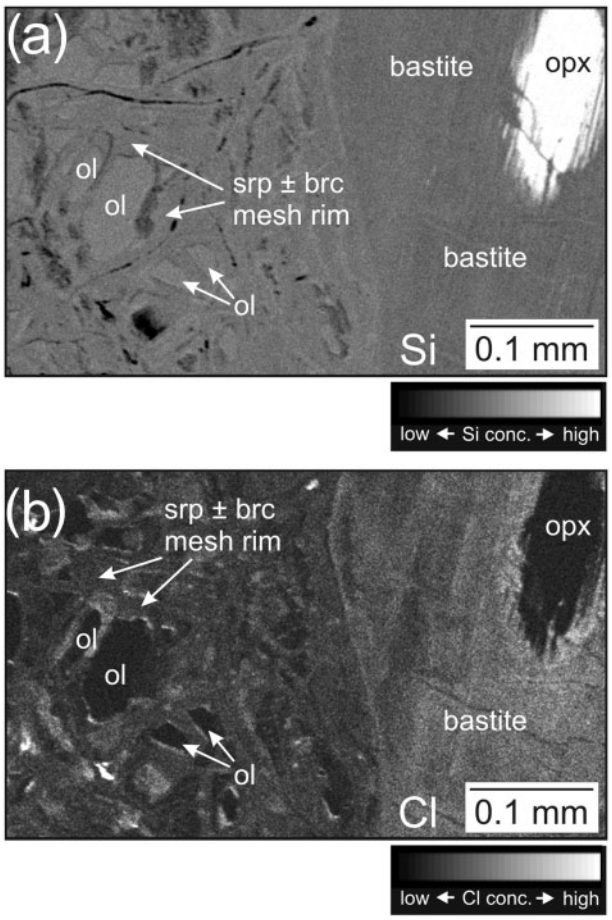

Fig. 11. Si (a) and Cl (b) distribution in serpentine ± brucite pseudomorphs. X-ray maps of sample S003 (MAR). Although Cl is detectable everywhere apart from olivine and orthopyroxene, point-like Cl sources are rare throughout the mapped area.

Selective trace element enrichments through serpentinization and carbonate precipitation

Bulk-rock serpentinites are conspicuously enriched in Cl and B relative to PM (Fig. 3). Moreover, Sr, Li, Sb, Pb, U, Rb and Cs are often enriched relative to elements of similar compatibility during mantle melting (Fig. 5). We now address the element-specific effects of serpentinization and carbonate precipitation and identify the host minerals of the enriched elements.

Chlorine

Bulk-rock Cl contents in the studied serpentinites (EA3) are 28–6l0 times PM concentrations (McDonough & Sun, 1995), demonstating that ocean floor serpentinites are the major host of Cl in the oceanic lithosphere, in line with previous observations (e.g. Scambelluri *et al.*, 1997; Sharp & Barnes, 2004; Bonifacie *et al.*, 2008). Cl abundance shows uneven spatial distribution in mesh rims and bastite. However, spots with an extremely high Cl signal that may indicate separate crystals of Cl-rich salts were observed only rarely in X-ray maps (Fig. 11a and b). Cl contents of pseudomorphic serpentine ± brucite [(3·2–1200) × PM] correlate well with bulk-rock Cl concentrations; however, brucite is generally Cl-poor compared with serpentine ± brucite (EA5). An exception to this trend is the brucite-rich (SiO_2 5·99–12·53 wt %) mesh center of S02l, which has a considerable Cl content (0·21–0·47 wt %; EA5). Together, these observations suggest that serpentine per se (without brucite or interstitial salts) is the most important host for Cl in most serpentinites, with Cl either bound in crystal lattices or loosely connected to crystal surfaces. Brucite may also be an important Cl-host, but only rarely. Alternatively, Cl may reside in a Cl-rich phase [e.g. $\alpha Mg_2(OH)_3Cl$ or $\alpha Fe_2(OH)_3Cl$; Rucklidge & Patterson, 1977] that forms intimate intergrowths with serpentine such that it appears to be a part of the serpentine-dominated pseudomorphs, similar to the serpentine + brucite intergrowths of the mesh rims and

centers (Fig. 6). In S004 (MAR) and S039 (Hess Deep), iowaite was also identified as a Cl-host in mesh rims and mesh centers (Table 2; EA5). However, intergrowths of chlorides with serpentine are unlikely to be present in bastite (owing to the higher activity of silica and the corresponding lower pH), which nevertheless contains thousands of $\mu g\,g^{-1}$ Cl (EA5). Thus, a substantial part of the Cl must reside in serpentine, even if chlorides may form intergrowths with it.

The lack of correlation between the Cl content and major element concentrations of pseudomorphic serpentine ± brucite (EA5) suggests that Cl incorporation is not a simple function of the chemical composition of the serpentine. However, the serpentine mineralogy appears to have an effect on Cl incorporation into serpentine, as demonstrated by the average nine times higher Cl concentrations in chrysotile- or lizardite-dominated pseudomorphic replacements and veins compared with those in antigorite (EA5).

Boron

B is the second most enriched trace element in serpentinites after Cl (EA3, Fig. 3). *In situ* trace element analysis indicates that most of the B resides in the pseudomorphic serpentine (EA5; Fig. 8). There are no significant differences between the B contents of lizardite- and chrysotile-dominated pseudomorphic replacements but, as with Cl, there is significantly less B in antigorite than in either chrysotile or lizardite. Antigorite forming veins in S025 (Hess Deep) has much lower B contents (0·76–3·6 $\mu g\,g^{-1}$) than vein filling lizardite in the same sample (39–61 $\mu g\,g^{-1}$; EA5).

Although serpentine is the major carrier of B in serpentinites, we note that aragonite may also contain substantial amounts of B (9·2–49 $\mu g\,g^{-1}$; EA5). This suggests that aragonite, if present, may significantly contribute to the bulk B content of serpentinites.

Serpentine ± brucite pseudomorphs after olivine contain about half the B (average 48 $\mu g\,g^{-1}$) of serpentine formed after orthopyroxene (average 98 $\mu g\,g^{-1}$) in MOR and Mariana fore-arc serpentinites, in contrast to Guatemala fore-arc and PaMa serpentine pseudomorphs, which do not show such a clear trend (EA5; Fig. 8). The possible causes of the observed texturally related differences in B abundance are discussed below.

(1) Pseudomorphic replacements after olivine often contain brucite whereas bastite does not (Fig. 6a). Thus, B-poor brucite (B < 1 $\mu g\,g^{-1}$; EA5) could dilute serpentine-hosted B in serpentine ± brucite mixtures replacing olivine. Mass-balance calculations demonstrate that 75–80 mol % brucite admixture to serpentine is required to lower its B content from 98 to 48 $\mu g\,g^{-1}$; that is, from the average B content of MOR and Mariana fore-arc bastite (chosen as the serpentine 'end member' of the mixture) to the average B content of mesh pseudomorphs in the same samples. However, such high brucite contents are inconsistent with our major element data on mesh rims and centers from these and other serpentinites, suggesting a maximum of 40 mol % brucite in the overwhelming majority of mesh pseudomorphs (EA5; Fig. 6b). Thus, brucite addition alone cannot explain the lower B concentrations of the mesh pseudomorphs.

(2) Elevated B contents in bastite relative to mesh serpentine could also be generated if hydration of orthopyroxene mostly preceded that of olivine in a rock-dominated system with successively decreasing access to a B-bearing serpentinization fluid. This is possible if hydration of orthopyroxene started at $T > 300$–$350^{\circ}C$. At these conditions orthopyroxene is not stable in a peridotite–H_2O system whereas olivine is (with its stability field moving towards higher temperatures with increasing amounts of H_2O; Hemley *et al.*, 1977*a*, 1977*b*; Allen & Seyfried, 2003; Palandri & Reed, 2004; McCollom & Bach, 2009). In addition, orthopyroxene hydrates faster than olivine (a trend that reverses as T decreases; Martin & Fyfe, 1970). High-T serpentinization of orthopyroxene could thus leave olivine with minor alteration while taking out significant amounts of B from the fluid. The remaining olivine could then be serpentinized at lower T by a fluid substantially depleted in B.

The absence of talc from the bastite in all but two samples does not contradict the above scenario (i.e. that hydration of orthopyroxene mostly preceded that of olivine). Based on stoichiometry and assuming an olivine/orthopyroxene ratio of four (corresponding to harzburgite), serpentinization of only 25% of the available olivine could provide the necessary Mg and Fe to buffer the increased Si concentrations imposed by 100% orthopyroxene dissolution (note, however, that orthopyroxene is not completely serpentinized even in the most hydrated samples). Thus, talc formation could be inhibited during high-T serpentinization in most cases even though olivine reacts more slowly and to a lesser extent than orthopyroxene.

Zoning in mesh rims or bastite compositions with respect to B, which could support explanation (2), was not observed on the spatial scale of our LA-ICP-MS measurements (>32 μm). The high variations in the B contents of pseudomorphic serpentine ± brucite from single MOR and Mariana fore-arc samples (EA5) may, however, reflect compositional changes in the B abundance of the serpentinization fluid(s).

The above serpentinization sequence implies that serpentinization at the localities where bastite has higher B contents than mesh serpentine started at considerable depths (i.e. several kilometres, where T was high enough for orthopyroxene to react faster) with the introduction of unreacted seawater or slab-fluid (possibly through cracks in MOR settings; see Andreani *et al.*, 2007) and proceeded

with successively less B in the serpentinization fluid owing to bastite crystallization and decreasing access to the relatively B-rich, unreacted fluid. The latter could be caused by, for example, the volume increase imposed by serpentinization (assuming mass conservative serpentinization) or the filling of pre-existing cracks by crystallization of serpentine veins. Alternatively, there was continuous access to B-bearing fluids during exhumation and cooling but the uptake of B by serpentine was significantly enhanced at higher T, a possibility contradicting experimental observations (Foustoukos *et al.*, 2008).

Consistent with the above discussion, published O isotope data on serpentinites from two of the localities with bastite containing much more B than mesh pseudomorphs (MAR and Hess Deep) suggest temperatures in excess of 300°C for the start of serpentinization (Früh-Green *et al.*, 1996; Barnes *et al.*, 2009). For the Mariana fore-arc South Chamorro seamount serpentinite clasts D'Antonio & Kristensen (2004) estimated serpentinization temperatures mostly below 300°C, based on the coexistence of Fe-rich brucite, lizardite and chrysotile in mesh pseudomorphs, which does not exclude a higher T for bastite formation.

If explanation (2) is valid, it is easier to explain why B enrichment in bastite relative to mesh pseudomorphs is less pronounced or even reversed (i.e. more B in mesh than in bastite) in PaMa serpentinites (EA5). Serpentinization may have happened at relatively low T at these localities (for Iberia PaMa serpentinites mostly <250°C; Beard & Hopkinson, 2000; Skelton & Valley, 2000). Under such relatively low-T conditions olivine hydration rates are comparable with or faster than those of orthopyroxene (Martin & Fyfe, 1970) and, hence, B contents of mesh serpentine are expected to be similar to or higher than those of bastite.

(3) The higher B concentrations observed in bastite can also be the result of crystallographic differences between mesh serpentine and bastite, not indicated by Raman spectroscopy (Table 3), which lead to preferential uptake of B into bastite even if the fluid composition (B content) or the T of hydration is the same. This explanation, therefore, does not require that orthopyroxene be serpentinized first at higher T than olivine. A combination of the above explanations or explanation (2) or (3) alone are all plausible in MOR settings and in the Mariana fore-arc and do not exclude each other.

Strontium

Bulk-rock Sr contents in the studied serpentinites are 0·02–270 times PM values (Fig. 5), and are elevated relative to elements with similar compatibility, as has been reported for other serpentinized ultramafic rocks (e.g. Stephens, 1997; Parkinson & Pearce, 1998; Niu, 2004; Paulick *et al.*, 2006). Sr enrichment is partly related to carbonate addition. Although calcite contains significantly less Sr than aragonite, its Sr content is still 1–2 orders of magnitude higher than that of serpentine (EA5). Therefore, carbonates are the major hosts of Sr in carbonate-bearing serpentinites, independent of the carbonate mineralogy.

Serpentine ± brucite pseudomorphs are strongly enriched in Sr relative to the phases they replace. This is best illustrated by the elevated Sr abundances in serpentine ± brucite pseudomorphs (0·13–23 μg g^{-1} Sr; EA5) after essentially Sr-free olivine (0·002–0·02 μg g^{-1}; EA4). Because clinopyroxene generally contains less Sr than pseudomorphic serpentine ± brucite (EA4 and 5) and is not abundant (<5 vol. % in all but one sample; Table 3), the major host for bulk-rock Sr in carbonate-free serpentinites is serpentine. This is illustrated in Fig. 12, where the bulk-rock Sr concentrations of carbonate-free samples are plotted against average *in situ* serpentine ± brucite data. The Sr contents of lizardite- and chrysotile-dominated serpentine pseudomorphs do not differ systematically, as also seen for B and Cl, but lizardite and chrysotile are enriched in Sr when compared with antigorite (EA5).

The concentration of Sr in bastite tends to be higher than in mesh centers and rims (EA5; Fig. 8), similar to B in MOR and Mariana fore-arc samples. Mass-balance calculations, similar to those applied for B, indicate that dilution of serpentine by 85–90 mol % brucite would be required to explain the Sr concentrations of the mesh rims and centers; that is, much more brucite than observed (Fig. 6b). Again, brucite addition alone cannot explain the lower Sr concentrations in mesh pseudomorphs than in bastite. Thus, in most cases the distribution of Sr between different pseudomorphs is likely to be governed by the same mechanisms as those influencing B distribution (see above).

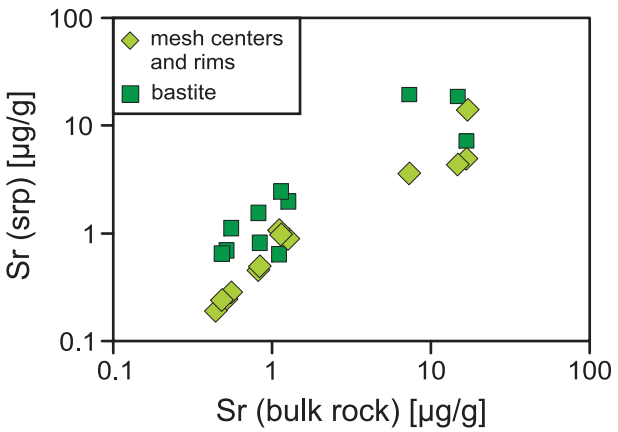

Fig. 12. Bulk-rock Sr concentrations in carbonate-free serpentinites (EA3) and average Sr contents of serpentine ± brucite pseudomorphs in the same samples. Samples S025 and S034 are also plotted, as the carbonate veins in these samples could be removed and did not affect the bulk-rock Sr concentrations.

Uranium

Bulk-rock U concentrations are highly variable between serpentinite samples, from below the PM estimate ($0{\cdot}023\ \mu g\ g^{-1}$; McDonough & Sun, 1995) to enrichments of >60 times PM (EA3; Fig. 5), consistent with data for serpentinized peridotites from mid-ocean ridges and ridge–transform systems (e.g. Niu, 2004; Paulick *et al.*, 2006). U enrichments in bulk-rock serpentinites are most prominent in near-surface samples and are restricted to the uppermost 40–60 m of the basement (Fig. 13). Our *in situ* data show that U is hosted by aragonite veins as well as by serpentine (EA5).

Aragonite can contain up to $4{\cdot}5\ \mu g\ g^{-1}$ U whereas the U content of calcite always remains below $0{\cdot}02\ \mu g\ g^{-1}$ (EA5), probably reflecting the higher affinity of the aragonite structure relative to that of calcite to host U (Reeder *et al.*, 2000). Carbonates found in serpentinites are thought to form near the surface through mixing of seawater and serpentinization-related fluids (e.g. Beard & Hopkinson, 2000; Mottl *et al.*, 2004; Ludwig *et al.*, 2006). Thus, carbonate-related U enrichment is expected in the uppermost parts of the basement, as also shown by our data (Tables 1 and 2; EA5; Fig. 13).

Previous observations have suggested that U enrichment in the uppermost parts of hydrated mafic and ultramafic rocks could be related to oxidative seafloor weathering, possibly by sorption of U on Fe-oxyhydroxides (Arnold *et al.*, 1998; Bach *et al.*, 2003; Krawczyk-Bärsch *et al.*, 2004). Although many of our U-rich serpentinites show evidence for iron-oxide precipitation owing to weathering (as seen in the Newfoundland serpentinites) we took care during *in situ* analysis to analyse clear domains of pseudomorphic and vein serpentine (devoid of iron oxides, hydroxides or carbonates), and we found that the observed U signal was related to serpentine. These analyses yielded U concentrations up to $3{\cdot}25\ \mu g\ g^{-1}$ (EA5).

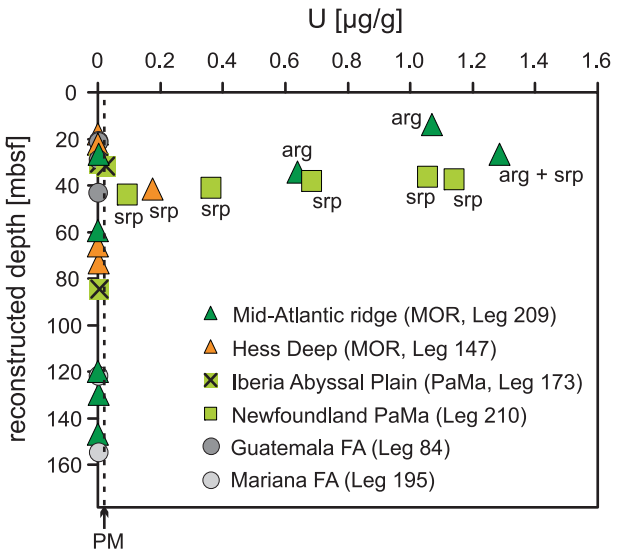

Fig. 13. Bulk-rock U concentrations of serpentinites as a function of depth below the sea floor at which they were drilled. Depth data (Table 1) were corrected for overlying sedimentary and other, surface-related rocks (e.g. basalt flows; see EA1 for further details). Dashed line shows the Primitive Mantle (PM; McDonough & Sun, 1995) concentration. Carrier phases of U in the most U-enriched samples are indicated next to the sample symbols. FA, fore-arc.

The experimental data of Singer *et al.* (2009) demonstrate that U sorption on chlorite, a mineral with a structure similar to that of serpentine, is not necesserally related to the precipitation of Fe-oxides or to the change in the oxidation state of U (reduction). U enrichment is therefore enhanced, but not necessarily caused, by a change in redox conditions. Elevated U concentrations found in serpentine are thus not necesserally related to weathering.

Moreover, two of the high-U serpentinites (S001 and S025) show little sign of weathering even though they were sampled at <60 mbsf (metres below sea floor; Table 1). For example, S025 ($U^{bulk-rock}$ $0{\cdot}18\ \mu g\ g^{-1}$, i.e. $8{\cdot}7 \times$ PM; U^{srp} up to $1{\cdot}8\ \mu g\ g^{-1}$; EA3 and 5) has characteristics consistent with a relatively high T of serpentinization (tremolite and antigorite in the hydrothermal alteration assemblage and relatively unaltered olivine together with highly serpentinized orthopyroxene; Tables 2 and 3) and it is also the least altered sample of all (degree of alteration 69 vol. %; Table 3), yet it was found at a depth between 40·7 and 41·5 mbsf. If such serpentinites really do represent deeper parts of the basement than the depth at which they were sampled, then it follows that either U enrichment may occur at greater depths than previously thought (e.g. Kelemen *et al.*, 2007; Morishita *et al.*, 2009) or serpentine can change its U content at shallow depths without visible recrystallization or growth of new minerals.

If the high U concentrations observed in serpentine ± brucite pseudomorphs were attained during serpentinization, then high-T hydrothermal alteration (in addition to weathering) can also influence U distribution in serpentinized ultramafic rocks. Evidence for U mobility during high-T hydration is also provided by the tremolite compositions in S039 (U^{tr} $0{\cdot}01\ \mu g\ g^{-1}$; $U^{cpx\ replaced\ by\ tr} < 0{\cdot}004$; EA4 and 5). Augustin *et al.* (2008) also observed hydrothermal U enrichment in serpentinites associated with the $T > 350°C$ Logatchev hydrothermal field on the Mid-Atlantic Ridge.

In summary, in samples where aragonite is not present or is not the only phase containing substantial amounts of U, U is spatially related to serpentine and not to weathering-related minerals, such as oxides, but it is not possible based on our data to tell whether it was introduced during serpentinization or during weathering. U enrichment of hydrating ocean-floor peridotites may start already during high-T serpentinization and amphibole growth.

Antimony and lead

We rely on bulk-rock data when discussing Sb and Pb behaviour during serpentinization because *in situ* Sb and Pb analyses are likely to have been influenced by contamination during sample preparation or analytical artefacts (see above). Both elements are significantly enriched in ocean floor and fore-arc serpentinites relative to elements of similar compatibility (Fig. 5), but their absolute concentrations are mostly at the ng g^{-1} to tens of ng g^{-1} level (EA3).

Relative enrichments in Sb are caused by serpentinization and/or carbonate precipitation. This is demonstrated by variations of Sb/Ce vs Sr/Pr (Fig. 14). All but three of our serpentinites have more than one order of magnitude higher Sb/Ce than that of the primitive or the depleted mantle. Partial melting or melt metasomatism is unlikely to account for this, because the compatibility of Sb and Ce is similar during mantle melting (Sims *et al.*, 1990). The positive correlation between Sb/Ce and Sr/Pr (similar to Sb and Ce, Sr and Pr are also similarly incompatible during mantle melting; Hofmann, 1988) in the studied serpentinites (Fig. 14) shows that enrichments in Sb and Sr are coupled, which suggests that Sb enrichments result from serpentinization and/or carbonate precipitation, as elevated Sr is hosted by serpentine and carbonate (see above). This premise also excludes sulphides as significant carriers of Sb. The positive correlation between Sb/Ce and Sr/Pr is shown clearly by carbonate-free serpentinites (Fig. 14), demonstrating that serpentinite is a major carrier of Sb, whereas carbonate-bearing samples display only a weak correlation (Fig. 14), possibly indicating that carbonates are not important hosts of Sb. However, carbonate (in particular calcite) can incorporate significant amounts of Ce and Pr (and other LREE; EA5), which can mask a positive correlation between Sb/Ce and Sr/Pr in serpentinites containing Sb and LREE-bearing carbonates. Indeed, Newfoundland samples containing LREE-bearing calcite as the carbonate phase cluster tightly in Fig. 14, whereas MAR samples containing (REE-poor) aragonite have increased Sr/Pr while maintaining about the same Sb/Ce as that of carbonate-free samples from the same locality. In conclusion, bulk-rock data suggest that the increased Sb content of serpentinites is hosted by serpentine and possibly by calcite, but not by aragonite.

Relative Pb enrichments (Fig. 5) in ocean floor and fore-arc serpentinites are only partly related to serpentinization and are unlikely to be influenced by carbonate precipitation. Similar to Sb, we tried to analyse relative Pb enrichment through comparison with Sr. Although the dataset as a whole shows a general positive correlation between Pb/Ce and Sr/Pr (Fig. 15), single localities display no clear correlation, with the exception of Hess Deep. This suggests that the relative enrichment in Pb is only partly related to that of Sr. Samples containing irremovable carbonates do not display a positive correlation between relative Pb and Sr enrichments (Fig. 15), which we take as evidence that carbonates are not significant carriers of Pb. Based on our data, sulphides (either relic

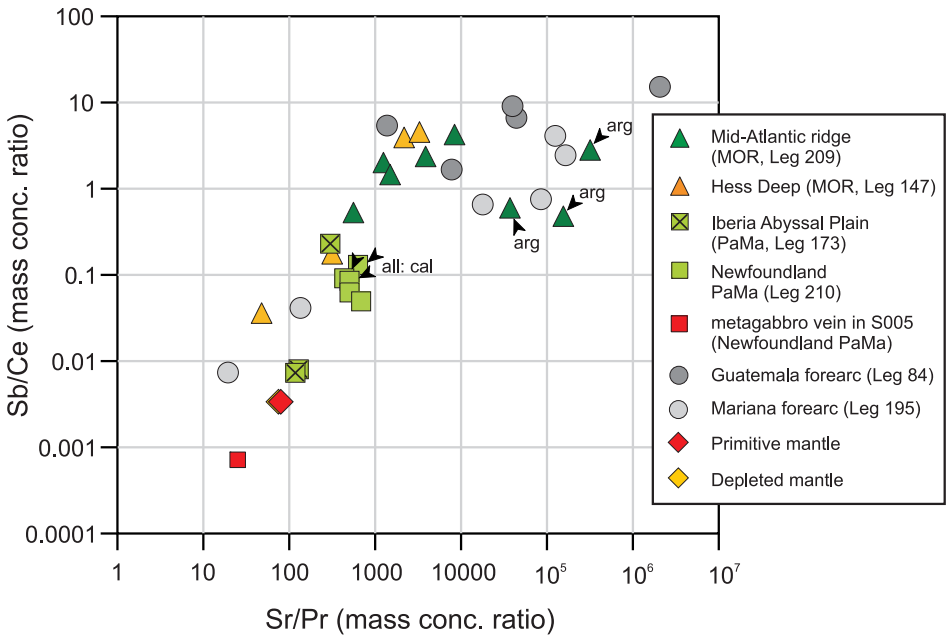

Fig. 14. Sr/Pr vs Sb/Ce in serpentinites and serpentine muds. Black arrowheads mark samples with significant amounts (i.e. several vol. %) of irremovable carbonate in the bulk-rock aliquots. Carbonate mineral type (calcite or aragonite) is also indicated. Primitive and depleted mantle compositions are from McDonough & Sun (1995) and Salters & Stracke (2004), respectively.

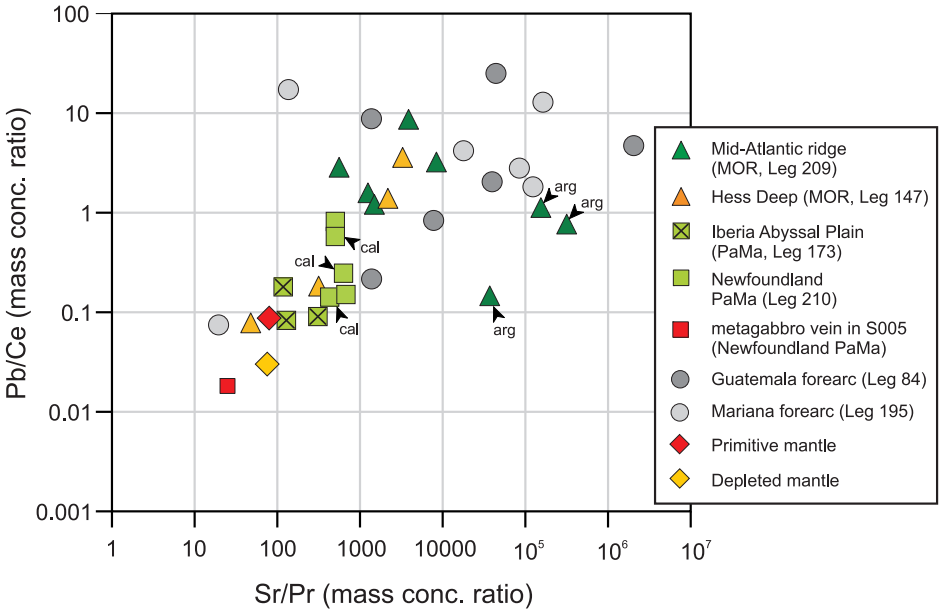

Fig. 15. Sr/Pr vs Pb/Ce of serpentinites and serpentine muds. Black arrowheads mark samples with significant amounts (i.e. several vol. %) of irremovable carbonate in the bulk-rock aliquots. Carbonate mineral type (calcite or aragonite) is also indicated. Primitive and depleted mantle compositions are from McDonough & Sun (1995) and Salters & Stracke (2004), respectively.

or hydration-related sulphides) may (also) be possible carriers of elevated Pb.

Cesium and rubidium

Cs and Rb both show elevated concentrations relative to elements of similar compatibility in most serpentinites, most prominently in Mariana fore-arc samples (Fig. 5). Rb and Cs contents of pseudomorphic serpentine ± brucite are higher than the Rb and Cs contents of olivine and orthopyroxene (EA4 and 5), which indicates that Rb and Cs enrichment occurred during serpentinization.

Rare earth elements

Mid-ocean ridge and fore-arc serpentinites have chondrite-normalized REE patterns with slight relative LREE enrichment and, with the exception of Mariana fore-arc samples, positive Eu anomalies (Fig. 4). As we found no REE-rich accessory phases in BSE images, we postulate that REE are hosted by the major rock-forming minerals. LREE enrichment and positive Eu anomalies can be generated by serpentinization but also by melt–rock interaction (see below; Niu, 2004; Paulick *et al.*, 2006).

A comparison of the REE patterns of orthopyroxene and bastite in S025 (Fig. 9c) suggests that the relative LREE enrichment and positive Eu anomalies of the Hess Deep serpentinites are largely related to serpentinization. Furthermore, Fig. 9d shows that early, high-T growth of tremolite (T presumably higher than *c.* 400°C; McCollom & Bach, 2009) at the expense of clinopyroxene (Fig. 1b) can also influence the REE distribution in ultramafic rocks hydrated on the ocean floor. The slight LREE enrichment and small positive Eu anomaly of most MAR samples could also be caused by serpentinization, as suggested by the bastite compositions in S003 (Fig. 9a), although our data are not conclusive because LREE and MREE abundances are mostly below the detection limit. Our findings are in line with those of Paulick *et al.* (2006) based on bulk serpentinite REE patterns, and further suggest that melt–rock reaction prior to serpentinization (e.g. S010) is not the only process responsible for LREE enrichment in these rocks (compare Seyler *et al.*, 2007).

Acidic fluids, like those emanating from MOR hydrothermal systems, have increased LREE/HREE and positive Eu anomalies, but have overall low REE contents (Michard, 1989; Douville *et al.*, 2002; Schmidt *et al.*, 2007). However, it is conceivable that even if REE-poor, such fluids can still affect the REE patterns of serpentinites because serpentinites as well as their protoliths are also depleted in REE. Relatively acidic solutions will evolve to alkaline compositions through interaction with ultramafic rocks if T is sufficiently low for olivine alteration ($T < 400$°C; e.g. Allen & Seyfried, 2003; Palandri & Reed, 2004). Increasing pH causes a drop in REE solubility (Michard, 1989), providing a mechanism for LREE and Eu enrichment during serpentine crystallization.

Serpentinization and geodynamic setting

The most important parameters influencing the trace element concentrations in ocean floor and fore-arc

serpentinites are (1) the petrological history of the precursor peridotites (e.g. degree of partial melting, refertilization), (2) the chemistry of the serpentinization fluid (dominantly seawater-derived fluids or fluids from a subducting lithospheric plate), (3) duration and temperature of seawater–peridotite interaction and (4) the amount and type of carbonate precipitated during and after exhumation. The relative significance and nature of these parameters is different in different geodynamic settings of serpentinization, such as mid-ocean ridges, passive margins or fore-arcs. As a consequence, serpentinites from these settings have slightly different geochemical characteristics, which we discuss below.

Mid-ocean ridges (MOR)

Strongly depleted trace element compositions (EA3; Fig. 5) characterize serpentinites from MOR environments in general, imposed by large fractions of (pre-serpentinization) melt extraction (15–18%; EA4). Cl and B are present in high concentrations (1280–6600 and 15–110 $\mu g\,g^{-1}$, respectively). U, Pb, Sb, Sr and Li also show relative enrichments (Fig. 5), although the concentrations of these elements mostly remain below those of Primitive Mantle (Fig. 5). The presence of aragonite in the uppermost 40–60 m of MOR serpentinites leads to the strongest U and Sr enrichments with concentrations more than 10 times Primitive Mantle estimates. Serpentinization and hydrothermal tremolite growth partly explain the U-shaped chondrite-normalized REE patterns and positive Eu anomalies of MOR serpentinites (Fig. 9a, c and d).

Passive margins (PaMa)

Passive margin serpentinites have generally higher incompatible trace element concentrations than MOR or fore-arc serpentinites (Fig. 5), because the PaMa peridotites had experienced smaller degrees of partial melting and/or had been more strongly refertilized by metasomatizing melts prior to serpentinization than peridotites from other settings. Consequently, the material available for serpentinization was of an overall less depleted chemical composition when compared with that present in MOR settings.

Passive margin serpentinites show the highest B contents (up to 170 ppm) among serpentinites from different settings, whereas their Cl contents are comparable with those of MOR serpentinites (EA3). Considering that serpentinization of PaMa peridotites may have happened largely at lower T (for Iberia PaMa <250°C; Beard & Hopkinson, 2000; Skelton & Valley, 2000) than along mid-ocean ridges (serpentinization started at $T > 350$°C; e.g. Früh-Green *et al.*, 1996), the high B concentrations of Pa Ma serpentinites may reflect the negative correlation between serpentinization temperature and B content (Bonatti *et al.*, 1984). Furthermore, the higher B contents of the PaMa serpentinites relative to those of MOR and fore-arc serpentinites (Fig. 3) may also reflect the higher fluid flux experienced by PaMa serpentinites during long exposure on, or near, the seafloor (e.g. in Newfoundland since Barremian times; Robertson, 2007) to seawater-derived fluids.

Bulk-rock Sr concentrations are significantly increased by serpentinization (i.e. >6 times higher Sr concentration in bastite than in orthopyroxene; e.g. S006, S008; EA4 and 5). The effect of carbonate addition on bulk-rock Sr contents is smaller than in the case of MOR serpentinites because the dominant carbonate type in PaMa serpentinites is calcite (Table 2), which contains less Sr than aragonite (EA5). In fact, a calcite-dominated carbonate mineralogy, and therefore lower levels of carbonate-hosted Sr, are expected in PaMa serpentinites, because they are exposed on or near the seafloor for millions of years, allowing most of the metastable aragonite (formed early during exhumation) to transform into calcite (Milliken & Morgan, 1996).

Fore-arcs

The studied fore-arc serpentinites have generally very low trace element concentrations (0·001–0·1 × PM; Fig. 5), similar to those of MOR serpentinites, reflecting high degrees of melting and melt extraction of the precursor peridotites (17–20%; EA4). Serpentine muds of the Mariana fore-arc show overall higher trace element contents than serpentinites, owing to the presence of fine-grained mafic rock fragments in the muds, which are trace element rich relative to the serpentine component of the mud (Savov *et al.*, 2005*b*).

The most distinctive compositional feature of fore-arc serpentinites is their generally strong bulk-rock enrichment in Cs and Rb along with Sr, Sb and Li relative to elements of similar compatibility (Fig. 5). Relative Sr enrichments are especially striking as only one of our fore-arc serpentinites contains potentially Sr-rich carbonate and gypsum (Table 2). The relative enrichments in Cs, Rb, Sr and Li are orders of magnitude higher than those displayed by carbonate-free MOR and PaMa serpentinites (e.g. Sr_N/Nd_N: 32–2400 and 0·85–140 for carbonate-free fore-arc and MOR serpentinites, respectively; Fig. 5). *In situ* data demonstrate that these enrichments are the product of serpentinization, as these elements (Cs, Rb, Sr and Li) are hosted by serpentine but not by its precursor olivine and orthopyroxene (EA4 and 5). Relative Sb enrichments are orders of magnitude higher than those found in PaMa serpentinites but generally comparable with those of MOR serpentinites and, based on bulk-rock data, are also related to serpentinization (see above; Fig. 14).

Increased concentrations of Cs, Rb, Sr, and sometimes Li in fore-arc relative to MOR samples are probably not the result of a higher affinity of these elements to enter serpentine during fore-arc serpentinization, because even

those fore-arc serpentinites that were hydrated under about the same temperature conditions as MOR samples show increased concentrations of LILE and Sr. For example, both S029 (Mariana fore-arc) and S033 (Hess Deep) have pseudomorphic replacements after olivine with a considerable amount of Fe-rich brucite (EA5), which indicates temperatures at or slightly above ~200°C when most of the olivine was hydrated (see McCollom & Bach, 2009). Nevertheless, mesh rims in the fore-arc sample S029 have >8 times more Cs, >28 times more Rb and ~38 times more Sr on average than the mesh rims in MOR sample S033 (EA5).

The high LILE and Sr contents of fore-arc serpentinites, therefore, probably indicate elevated concentrations of these elements in the fore-arc hydration fluids when compared with hydration fluid compositions in MOR or PaMa settings. Fluids with elevated LILE, Sr and Li contents (i.e. near or above seawater values) are expected to be released from sediments during shallow subduction (You *et al.*, 1996) (i.e. beneath fore-arcs). Thus, most of the studied fore-arc serpentinites could have interacted with fluids that, at least partially, equilibrated with or were derived from sediments in fore-arc settings, consistent with a subducting plate origin of fore-arc fluids (e.g. Fryer *et al.*, 1985). The two Guatemala fore-arc samples showing LILE enrichments similar to those observed in Mariana fore-arc serpentinites (Fig. 5) potentially indicate that serpentinizing fluids with similar chemistry (high LILE and Sr contents relative to MOR serpentinizing fluids) may occur in different fore-arc settings.

Variations in the LILE, Sr, Ba and Li contents of pseudomorphic serpentine ± brucite within single fore-arc samples (e.g. S017, S030, S032) are often too high to be consistent with hydration and trace element enrichment owing to a single fluid infiltration event, leading to the formation of serpentine with successively lower trace element contents as hydration proceeds. For example, we see 8·3–33 $\mu g\,g^{-1}$ Li in the serpentine pseudomorphs of S030, even though the distribution coefficients for Li between serpentine and associated fluids are <1 under fore-arc P–T conditions (Wunder *et al.*, 2010) and serpentinization consumes H_2O, which together make it impossible to deplete a fluid in Li through a reaction with dry peridotite (even though the absolute amount of Li stored in the hydrated rocks can be considerable). Interestingly, the entire range of Li contents found in the serpentine of S030 can be encountered within a distance of 2 mm and for the same textural type of serpentine (mesh rims). Thus, the observed variations in the Li content of serpentine in S030 can be explained only by temporal variations in fluid chemistry. It is possible that the large variations in Li and Rb contents of pseudomorphic serpentine within S017 (Guatemala fore-arc) also reflect temporal variations in the chemistry of the serpentinizing fluids. Our findings suggest that, even though the chemistry of fluids metasomatizing the fore-arc mantle wedge can be different, as shown by the millimetre-scale variations in serpentine chemistry, bulk serpentinites 'average out' these different chemical signals before potential transport to sub-arc depths (Tatsumi, 1989; Savov *et al.*, 2007).

Potential effects of ocean floor serpentinites on subduction zone chemical cycling

Our new dataset constrains the chemical signatures of ocean floor and fore-arc serpentinites entering subduction zones. Thus, we provide inputs to models that simulate the chemical evolution of fluids released during progressive serpentinite subduction and try to identify possible components enriching arc magma sources in certain trace elements (e.g. Singer *et al.*, 2007; Tonarini *et al.*, 2007).

High bulk-rock Cl and B concentrations (up to 6600 $\mu g\,g^{-1}$ and 170 $\mu g\,g^{-1}$, respectively; EA3) combined with the potentially large fraction of serpentinite in the subducting oceanic lithosphere (up to 20% in the uppermost 20 km; Ranero & Sallarés, 2004) and in the fore-arc mantle wedge (15–30%; Hyndman & Peacock, 2003) make ocean-floor and fore-arc serpentinites important carriers of these elements into subduction zones (see also Scambelluri *et al.*, 2004; Barnes *et al.*, 2008; Vils *et al.*, 2008). However, serpentinite Cl and B contents vary considerably (i.e. 470–6600 and 5·4–170 $\mu g\,g^{-1}$, respectively; EA3) among and within serpentinites from specific tectonic settings, rendering it difficult to establish a quantitative ocean floor serpentinite contribution to subduction zone Cl and B cycling. The relative significance of the different serpentinization settings is clearly indicated, however. For example, based on our data, the same mass of subducted PaMa serpentinite is expected to deliver significantly more B on average into a subduction zone than, for example, a MOR serpentinite.

Carbonate-bearing serpentinites can carry significant amounts of Sr and U into subduction zones (EA3 and 5). In the absence of experimental data on carbonate stability and corresponding fluid compositions in hydrated ultramafic rocks in the P–T range relevant for serpentinite dehydration in subduction zones, we cannot predict the amount of dissolvable carbonate in dehydrating serpentinites. However, by analogy with mafic rocks, it is expected to decrease with increasing pressure (Molina & Poli, 2000). Thus, serpentinite-hosted carbonates remaining stable beyond sub-arc depths may be important in mantle-scale recycling of Sr and U by delivering substantial amounts of these elements back to the mantle.

Owing to the very low overall trace element and especially HFSE and REE concentrations in most serpentinites (EA3), the enrichments in Sr, U, Sb, Pb, Rb, Cs and Li relative to elements of similar compatibility during

mantle melting (i.e. $Sr_N/Nd_N = 1–140$ in carbonate-free serpentinites, median = 30; $U_N/Th_N = 1–1900$ in carbonate-free serpentinites, median = 6; $Sb_N/Ce_N = 3–2800$ in carbonate-free serpentinites, median = 570; $Pb_N/Ce_N = 0·9–280$ in all analysed serpentinites, median = 20; $Li_N/Y_N = 2–6400$ in all analysed serpentinites, median = 30) are mostly higher than those seen in other subducted components, such as oceanic sediments (Sr_N/Nd_N 0·1–6; U_N/Th_N 0·3–6; Pb_N/Ce_N 1·5–14, Plank & Langmuir, 1998; Sb_N/Ce_N 1–30; Li_N/Y_N 1·2–11, Bouman *et al.*, 2004) or altered igneous oceanic crust (AOC; Sr_N/Nd_N 0·2–5; U_N/Th_N 0·2–8; Pb_N/Ce_N 0·1–2·3, Hart *et al.*, 1999; Sb_N/Ce_N 1–1200, median = 43, Jochum & Verma, 1996; Li_N/Y_N 40–210, Kelley *et al.*, 2003). This suggests that serpentinites dehydrating in subduction zones could be sources of some of the characteristic trace element enrichments seen in arc volcanic rocks (e.g. high B_N/Nb_N, high Sr_N/Nd_N, high Sb_N/Ce_N; Moriguti *et al.*, 2004; Noll *et al.*, 1996), provided that large amounts of serpentinite dehydrate at sub-arc depths relative to the amount of dehydrating sediments and AOC and that the relative trace element enrichments shown by serpentinites are maintained (or increased) during prograde metamorphism. We now examine whether these conditions are realized.

Serpentinite dehydration in the subducting lithosphere can induce partial melting in the overlying sediments by flushing them with large amounts of H_2O-rich fluid, should temperatures exceed their wet solidi. In this case, the trace element signals carried by the serpentinite dehydration fluids are modified by those of the partial melts. High B/Nb, B/Th, U/Th, Sb/Ce, Pb/Ce, Sr/Nd and Li/Y potentially produced by serpentinite-derived fluids will be lowered through mixing with partial melts of the sediments, characterized by increased HFSE, Ba and REE contents, rendering serpentinite dehydration less noticeable in arc magma trace element distribution patterns or leading to correlations between those trace element ratios of arc magmas that are predominantly influenced by the partial melts of sediments and those influenced by serpentinite-derived fluids. Even without considering partial melting of metasediments, it is likely that fluids released by serpentinites, sediments or the AOC of the downgoing plate mix to a considerable extent before entering the mantle wedge (e.g. King *et al.*, 2006). Consequently, the trace element ratios of arc volcanic rocks and possible correlations among them do not discriminate dehydrating ocean floor serpentinites (or other subducted components) unequivocally as the fluid sources for mantle metasomatism, even though serpentinites are the most important sources of H_2O for mantle wedge metasomatism and may play an important role in global element cycling.

In this respect fore-arc serpentinites dragged down to sub-arc depths (e.g. Tatsumi, 1989) are of particular interest, because fluids produced by their dehydration are expected to be less modified through mixing with sediment- and/or AOC-derived fluids or melts. Our data indicate that fore-arc serpentinites have the highest concentrations of, and show the highest relative enrichments in, Sr, Rb and Cs (Fig. 5; EA3) among serpentinites from different geodynamic settings. Thus, fore-arc serpentinites may contribute to the relative LILE and Sr enrichment of arc magmas with minimal dilution from fluids or melts derived from sediments or AOC.

Our data suggest that subducted serpentinites are likely to produce fluids with characteristic enrichments in certain trace elements (i.e. high B/Nb, B/Th, U/Th, Sr/Nd, Sb/Ce, Pb/Ce and Li/Y) during subduction-related dehydration. Given the potentially high mass of subducted serpentinites (e.g. Ranero & Sallarés, 2004), serpentinites may play an important role in the global cycling of Cl, B, U, Sr (and, to a lesser extent, in the cycling of Sb, Pb and Li) through subduction zones; for example, by carrying significant amounts of these elements beyond sub-arc mantle depths, as can be imagined for serpentinites inside subducting cold oceanic plates (see Hacker, 2008). However, the relative contribution of serpentinites to arc magma sources with respect to most of these elements may be decreased by potential changes in serpentinite chemistry upon progressive partial dehydration (Scambelluri *et al.*, 2004) and by the contribution from subducted crustal components. The contribution of dehydrating serpentinites to the trace element inventory of arc magma sources becomes more evident in the case of those elements (e.g. Cl, B; Tonarini *et al.*, 2007; Barnes *et al.*, 2008) for which the contribution of sediment- and/or AOC-derived fluids and/or melts is minimal relative to that of serpentinites.

CONCLUSIONS

Serpentinites sampled at mid-ocean ridges, passive margins and fore-arcs represent ultramafic rocks with a complex history of strong melt depletion and sometimes melt metasomatism, followed by selective trace element enrichment during hydration on the ocean floor and in the fore-arc. Although serpentinites retain refractory bulk-rock major element compositions (apart from their elevated H_2O contents), they show up to several orders of magnitude enrichment in Cl, B, Sr, U, Sb, Pb, Rb, Cs and Li relative to elements of similar compatibility during mantle melting.

Enrichments in Cl, B, Sr, U, Sb, Rb, Cs and sometimes in Li are related to serpentinization. If present, carbonates host significant amounts of Sr and sometimes also U. Brucite, associated with serpentine replacements after olivine, is poor in trace elements.

Serpentinites show compositional variability as a function of the tectonic setting of the serpentinization.

Serpentinites from mid-ocean ridge environments are characterized by high relative enrichments in Cl, B, U, Sr, Sb, Pb and Li superimposed on overall strongly depleted trace element compositions. Passive margin serpentinites show the highest B contents and prominent U enrichments, with a generally less-depleted precursor composition. Fore-arc serpentinites are similar to mid-ocean ridge serpentinites with respect to their overall trace element depletion, as well as B, Sb, Pb and Li enrichment, but lack the U enrichment commonly observed in mid-ocean ridge and passive margin serpentinites. Fore-arc serpentinites also display smaller Cl and higher Cs, Rb and Sr enrichments than other serpentinites.

Serpentinites are the most important carriers of H, Cl and B into subduction zones when compared with other subducted components, such as sediments or altered igneous oceanic crust. In addition, carbonate-bearing serpentinites can provide Sr and U for arc magma source regions and/or they can deliver these elements to the lower mantle.

Serpentinites, although showing generally lower trace element abundances than oceanic crustal lithologies, are characterized by the highest primitive mantle-normalized B/Nb, B/Th, U/Th, Sb/Ce, Sr/Nd and Li/Yamong the subducted lithologies of the oceanic lithosphere (serpentinites, sediments and altered igneous crust). This is a consequence of the initially highly depleted nature of their mantle protoliths. Extreme relative trace element enrichment of the mantle wedge by the addition of fluids produced by serpentinite dehydration makes serpentinites one of the potential sources of some of the characteristic trace element signatures observed in arc magmas (e.g. high B/Nb, high U/Th, high Sr/Nd, high Sb/Ce). However, such a serpentinite imprint can be masked considerably by the trace element signal of subducted crustal components assimilated by serpentinite-derived fluids en route to the mantle wedge.

ACKNOWLEDGEMENTS

This research used samples provided by the Deep Sea Drilling Project and Ocean Drilling Program, which are sponsored by funding agencies of the participating countries under management of Joint Oceanographic Institutions (JOI), Inc. We are grateful to Lydia Zehnder and Peter Ulmer (ETH Zürich) for their help with the XRF sample preparation and measurements. The manuscript greatly benefited from the thorough reviews by Jun-Ichi Kimura, Ivan Savov and an anonymous reviewer. János Kodolányi is grateful to the members of the Department of Nuclear Research (Institute of Isotopes, Hungarian Academy of Sciences) for their hospitality during PGAA measurements, and to Marlina Elburg and Ingrid Smet for helping to improve the paper with their comments.

FUNDING

This work was supported by the Swiss National Science Foundation (PP002-106569 to T.P.; 200021-103479/1 for the use of the electron microprobe), the Canada Research Chairs Program (solution ICP-MS analyses) and the Seventh Framework Program of the European Union (NMI3: BRR 206; PGA analyses at the Budapest Neutron Centre).

SUPPLEMENTARY DATA

Supplementary data for this paper are available at *Journal of Petrology* online (http://www.petrology.oxfordjournals.org).

REFERENCES

Agranier, A., Lee, C.-T. A., Li, Z.-X. A. & Leeman, W. P. (2007). Fluid-mobile element budgets in serpentinized oceanic lithospheric mantle: Insights from B, As, Li, Pb, PGEs and Os isotopes in the Feather River Ophiolite, California. *Chemical Geology* **245**, 230–241.

Agrinier, P., Cornen, G. & Beslier, M.-O. (1996). Mineralogical and oxygen isotopic features of serpentinites recovered from the ocean/continent transition in the Iberia abyssal plain. In: Whitmarsh, R. B., Sawyer, D. S., Klaus, A. & Masson, D. G. (eds) *Proceedings of the Ocean Drilling Program, Scientific Results, 149.* College Station, TX: Ocean Drilling Program, pp. 541–552.

Allen, D. E. & Seyfried, W. E., Jr (2003). Compositional controls on vent fluids from ultramafic-hosted hydrothermal systems at midocean ridges: An experimental study at 400°C, 500 bars. *Geochimica et Cosmochimica Acta* **67**, 1531–1542.

Alt, J. C. & Shanks, W. C., III (2003). Serpentinization of abyssal peridotites from the MARK area, Mid-Atlantic Ridge: Sulfur geochemistry and reaction modeling. *Geochimica et Cosmochimica Acta* **67**, 641–653.

Andreani, M., Mével, C., Boullier, A.-M. & Escartín, J. (2007). Dynamic control on serpentine crystallization in veins: Constraints on hydration processes in oceanic peridotites. *Geochemistry, Geophysics, Geosystems* **8**, doi:10.1029/2006GC001373.

Arai, S. & Matsukage, K. (1996). Petrology of the gabbro–troctolite–peridotite complex from Hess Deep, equatorial Pacific: Implications for mantle–melt interaction within the oceanic lithosphere. In: Mével, C., Gillis, K. M., Allan, J. F. & Meyer, P. S. (eds) *Proceedings of the Ocean Drilling Program, Scientific Results, 147.* College Station, TX: Ocean Drilling Program, pp. 135–155.

Arnold, T., Zorn, T., Bernhard, G. & Nitsche, H. (1998). Sorption of uranium(VI) onto phyllite. *Chemical Geology* **151**, 129–141.

Augustin, N., Lackschewitz, K. S., Kuhn, T. & Devey, C. W. (2008). Mineralogical and chemical mass changes in mafic and ultramafic rocks from the Logatchev hydrothermal field (MAR 15°N). *Marine Geology* **256**, 18–29.

Auzende, A.-L., Daniel, I., Reynard, B., Lemaire, C. & Guyot, F. (2004). High-pressure behaviour of serpentine minerals: a Raman spectroscopic study. *Physics and Chemistry of Minerals* **31**, 269–277.

Babechuk, M. G., Kamber, B. S., Greig, A., Canil, D. & Kodolányi, J. (2010). The behaviour of tungsten during mantle melting revisited with implications for planetary differentiation time scales. *Geochimica et Cosmochimica Acta* **74**, 1448–1470.

Bach, W., Peucker-Ehrenbrink, B., Hart, S. R. & Blusztajn, J. S. (2003). Geochemistry of hydrothermally altered oceanic crust: DSDP/ODP Hole 504B—Implications for seawater–crust exchange budgets and Sr- and Pb-isotopic evolution of the mantle. *Geochemistry, Geophysics, Geosystems* **4**, doi:10.1029/2002GC000419.

Barnes, J. D. & Sharp, Z. D. (2005). A chlorine isotope study of DSDP/ODP serpentinized ultramafic rocks: Insights into the serpentinization process. *Chemical Geology* **228**, 246–265.

Barnes, J. D., Sharp, Z. D. & Fischer, T. P. (2008). Chlorine isotope variations across the Izu–Bonin–Mariana arc. *Geology* **36**, 883–886.

Barnes, J. D., Paulick, H., Sharp, Z. D., Bach, W. & BeauDoin, G. (2009). Stable isotope ($\delta^{18}O$, δD, $\delta^{37}Cl$) evidence for multiple fluid histories in mid-Atlantic abyssal peridotites (ODP Leg 209). *Lithos* **110**, 83–94.

Beard, J. S. & Hopkinson, L. (2000). A fossil, serpentinization-related hydrothermal vent, Ocean Drilling Program Leg 173, Site 1068 (Iberia Abyssal Plain): Some aspects of mineral and fluid chemistry. *Journal of Geophysical Research* **105(B7)**, 16527–16539.

Belgya, T. & Révay, Zs. (2004). Gamma-ray spectrometry. In: Molnár, G. L. (ed.) *Handbook of Prompt Gamma Activation Analysis with Neutron Beams*. Dordrecht: Kluwer Academic, pp. 71–111.

Bideau, D., Hebert, R., Hekinian, R. & Cannat, M. (1991). Metamorphism of deep-seated rocks from the Garrett ultrafast transform (East Pacific Rise) near 13°25'S. *Journal of Geophysical Research* **96(B6)**, 10079–10099.

Bonatti, E. (1976). Serpentinite protrusions in the oceanic crust. *Earth and Planetary Science Letters* **32**, 107–113.

Bonatti, E., Lawrence, J. R. & Morandi, N. (1984). Serpentinization of oceanic peridotites—temperature-dependence of mineralogy and boron content. *Earth and Planetary Science Letters* **70**, 88–94.

Bonifacie, M., Busigny, V., Mével, C., Philippot, P., Agrinier, P., Jendrzejewski, N., Scambelluri, M. & Javoy, M. (2008). Chlorine isotopic composition in seafloor serpentinites and high-pressure metaperidotites. Insights into oceanic serpentinization and subduction processes. *Geochimica et Cosmochimica Acta* **72**, 126–139.

Bouman, C., Elliott, T. & Vroon, P. Z. (2004). Lithium inputs to subduction zones. *Chemical Geology* **212**, 59–79.

Burgath, K. P., Marchig, V. & Mussallam, K. (1997). Data report: mineralogic, structural, and chemical variability of mantle sections from holes 920B and 920D. In: Karson, J. A., Cannat, M., Miller, D. J. & Elthon, D. (eds) *Proceedings of the Ocean Drilling Program, Scientific Results, 153*. College Station, TX: Ocean Drilling Program, pp. 521–505.

Carlson, R. L. (2001). The abundance of ultramafic rocks in Atlantic Ocean crust. *Geophysical Journal International* **144**, 37–48.

Cherniak, D. J. (2010). REE diffusion in olivine. *American Mineralogist* **95**, 362–368.

Contreras-Reyes, E., Grevemeyer, I., Flueh, E. R. & Scherwath, M. (2007). Alteration of the subducting oceanic lithosphere at the southern central Chile trench–outer rise. *Geochemistry, Geophysics, Geosystems* **8**, doi:10.1029/2007GC001632.

D'Antonio, M. & Kristensen, M. B. (2004). Serpentine and brucite of ultramafic clasts from the South Chamorro Seamount (Ocean Drilling Program Leg 195, Site 1200): inferences for the serpentinization of the Mariana forearc mantle. *Mineralogical Magazine* **68**, 887–904.

Decitre, S., Deloule, E., Reisberg, L., James, R., Agrinier, P. & Mével, C. (2002). Behavior of Li and its isotopes during serpentinization of oceanic peridotites. *Geochemistry, Geophysics, Geosystems* **3**, doi:10.1029/2001GC000178.

Dick, H. J. B. & Natland, J. H. (1996). Late-stage melt evolution and transport in the shallow mantle beneath the East Pacific Rise. In: Mével, C., Gillis, K. M., Allan, J. F. & Meyer, P. S. (eds) *Proceedings of the Ocean Drilling Program, Scientific Results, 147*. College Station, TX: Ocean Drilling Program, pp. 103–134.

Di Nicola, L., Schnabel, C., Wilcken, K. M. & Gméling, K. (2009). Determination of chlorine concentrations in whole rock: Comparison between prompt-gamma activation and isotope-dilution AMS analysis. *Quaternary Geochronology* **4**, 501–507.

Dohmen, R., Kasemann, S. A., Coogan, L. & Chakraborty, S. (2010). Diffusion of Li in olivine. Part I: Experimental observations and a multi-species diffusion model. *Geochimica et Cosmochimica Acta* **74**, 274–292.

Douville, E., Charlou, J. L., Oelkers, E. H., Bienvenu, P., Jove Colon, C. F., Donval, J. P., Fouquet, Y., Prieur, D. & Appriou, P. (2002). The rainbow vent fluids (36°14'N, MAR): the influence of ultramafic rocks and phase separation on trace metal content in Mid-Atlantic Ridge hydrothermal fluids. *Chemical Geology* **184**, 37–48.

Eggins, S. M., Woodhead, J. D., Kinsley, L. P. J., Mortimer, G. E., Sylvester, P., McCulloch, M. T., Hergt, J. M. & Handler, M. R. (1997). A simple method for the precise determination of > 40 trace elements in geological samples by ICPMS using enriched isotope internal standardisation. *Chemical Geology* **134**, 311–326.

Falloon, T. J., Green, D. H., Hatton, C. J. & Harris, K. L. (1988). Anhydrous partial melting of a fertile and depleted peridotite from 2 to 30 kb and application to basalt petrogenesis. *Journal of Petrology* **29**, 1257–1282.

Foustoukos, D. I., Savov, I. P. & Janecky, D. R. (2008). Chemical and isotopic constraints on water/rock interactions at the Lost City hydrothermal field, 30°N Mid-Atlantic Ridge. *Geochimica et Cosmochimica Acta* **72**, 5457–5474.

Früh-Green, G. L., Plas, A. & Lécuyer, C. (1996). Petrologic and stable isotope constraints on hydrothermal alteration and serpentinization of the EPR shallow mantle at Hess Deep (Site 895). In: Mével, C., Gillis, K. M., Allan, J. F. & Meyer, P. S. (eds) *Proceedings of the Ocean Drilling Program, Scientific Results, 147*. College Station, TX: Ocean Drilling Program, pp. 255–291.

Fryer, P. (2002). Recent studies of serpentinite occurrences in the oceans: mantle–ocean interactions in the plate tectonic cycle. *Chemie der Erde* **62**, 257–302.

Fryer, P., Ambos, E. L. & Hussong, D. M. (1985). Origin and emplacement of Mariana forearc seamounts. *Geology* **13**, 774–777.

Gméling, K., Harangi, Sz. & Kasztovszky, Zs. (2005). Boron and chlorine concentration of volcanic rocks: An application of prompt gamma activation analysis. *Journal of Radioanalytical and Nuclear Chemistry* **265**, 201–212.

Groppo, C., Rinaudo, C., Cairo, S., Gastaldi, D. & Compagnoni, R. (2006). Micro-Raman spectroscopy for a quick and reliable identification of serpentine minerals from ultramafics. *European Journal of Mineralogy* **18**, 319–329.

Guillong, M. & Heinrich, C. A. (2007). Sensitivity enhancement in laser ablation ICP-MS using small amounts of hydrogen in the carrier gas. *Journal of Analytical Atomic Spectrometry* **22**, 1488–1494.

Günther, D. & Hattendorf, B. (2005). Solid sample analysis using laser ablation inductively coupled plasma mass spectrometry. *Trends in Analytical Chemistry* **24**, 255–265.

Hacker, B. R. (2008). H_2O subduction beyond arcs. *Geochemistry, Geophysics, Geosystems* **9**, doi:10.1029/2007GC001707.

Hart, S. R., Blusztajn, J., Gick, H. J. B., Meyer, P. S. & Muehlenbachs, K. (1999). The fingerprint of seawater circulation in a 500-meter section of ocean crust gabbros. *Geochimica et Cosmochimica Acta* **63**, 4059–4080.

Hattori, K. H. & Guillot, S. (2003). Volcanic fronts form as a consequence of serpentinite dehydration in the forearc mantle wedge. *Geology* **31**, 525–528.

Hattori, K. H. & Guillot, S. (2007). Geochemical character of serpentinites associated with high- to ultrahigh-pressure metamorphic rocks in the Alps, Cuba, and the Himalayas: Recycling of elements

in subduction zones. *Geochemistry, Geophysics, Geosystems* **8**, doi:10.1029/2007GC001594.

Hattori, K. H., Takahashi, Y., Guillot, S. & Johanson, B. (2005). Occurrence of arsenic (V) in fore-arc mantle serpentinites based on X-ray absorption spectroscopy study. *Geochimica et Cosmochimica Acta* **69**, 5585–5596.

Hébert, R., Gueddari, K., Lafléche, M. R., Beslier, M. O. & Gardien, V. (2001). Petrology and geochemistry of exhumed peridotites and gabbros at non-volcanic margins: ODP Leg 173 West Iberia ocean–continent transition zone. In: Wilson, R. C. L., Whitmarsh, R. B., Taylor, B. & Froitzheim, N. (eds) *Non-Volcanic Rifting of Continental Margins: A Comparison of Evidence from Land and Sea. Geological Society*, . London: Special Publications **187**161–189.

Hellebrand, E., Snow, J. E., Dick, H. J. B. & Hofmann, A. W. (2001). Coupled major and trace elements as indicators of the extent of melting in mid-ocean-ridge peridotites. *Nature* **410**, 677–681.

Helm, R. (1985). Mineralogy and geochemistry of weathered serpentinites, Deep Sea Drilling Project Leg 84. In: von Huene, R. & Aubouin, J. *et al.* (eds) *Proceedings of the Deep Sea Drilling Project, Initial Reports, 84*. Washington, DC: US Government Printing Office, pp. 595–607.

Hemley, J. J., Montoya, J. W., Christ, C. L. & Hostetler, P. B. (1977*a*). Mineral equilibria in the MgO–SiO_2–H_2O system: I Talc–chrysotile–forsterite–brucite stability relations. *American Journal of Science* **277**, 322–351.

Hemley, J. J., Montoya, J. W., Shaw, D. R. & Luce, R. W. (1977*b*). Mineral equilibria in the MgO–SiO_2–H_2O system: I Talc–antigorite–forsterite–anthophyllite–enstatite stability relations and some geological implications in the system. *American Journal of Science* **277**, 353–383.

Hofmann, A. W. (1988). Chemical differentiation of the Earth: the relationship between mantle, continental crust, and oceanic crust. *Earth and Planetary Science Letters* **90**, 297–314.

Hyndman, R. D. & Peacock, S. M. (2003). Serpentinization of the forearc mantle. *Earth and Planetary Science Letters* **212**, 417–432.

Jackson, S. E. (2008). Lamtrace data reduction software for LA-ICP-MS. In: Sylvester, P. (ed.) *Laser Ablation ICP-MS in the Earth Sciences: Current Practices and Outstanding Issues. Mineralogical Association of Canada Short Course Series* **40**, 305–307.

Janecky, D. R. & Seyfried, W. E., Jr (1986). Hydrothermal serpentinization of peridotite within the oceanic crust: Experimental investigations of mineralogy and major element chemistry. *Geochimica et Cosmochimica Acta* **50**, 1357–1378.

Jaques, A. L. & Green, D. H. (1980). Anhydrous melting of peridotite at 0–15 kb pressure and the genesis of tholeiitic basalts. *Contributions to Mineralogy and Petrology* **73**, 287–310.

Jochum, K. P. & Verma, S. P. (1996). Extreme enrichment of Sb, Tl and other trace elements in altered MORB. *Chemical Geology* **130**, 289–299.

Karson, J. A. & Lawrence, R. M. (1997). Tectonic setting of serpentinite exposures on the western median valley wall of the MARK area in the vicinity of site 920. In: Karson, J. A., Cannat, M., Miller, D. J. & Elthon, D. (eds) *Proceedings of the Ocean Drilling Program, Scientific Results, 153*. College Station, TX: Ocean Drilling Program, pp. 5–21.

Kelemen, P. B., Kikawa, E. Miller, D. J. & Shipboard Scientific Party (2007). Leg 209 summary: processes in a 20-km-thick conductive boundary layer beneath the Mid-Atlantic Ridge, 14°–16°N. In: Kelemen, P. B., Kikawa, E. & Miller, D. J. (eds) *Proceedings of the Ocean Drilling Program, Scientific Results*, . College Station, TX: Ocean Drilling Program **209**, doi:10.2973/odp.proc.sr.209.001.2007.

Kelley, D. S., Plank, T., Ludden, J. & Staudigel, H. (2003). Composition of altered oceanic crust at ODP Sites 801 and 1149. *Geochemistry, Geophysics, Geosystems* **4**, doi:10.1029/2002GC000435.

King, R. L., Bebout, G. E., Moriguti, T. & Nakamura, E. (2006). Elemental mixing systematics and Sr–Nd isotope geochemistry of mélange formation: Obstacles to identification of fluid sources to arc volcanic. *Earth and Planetary Science Letters* **246**, 288–304.

Kodolányi, J. & Pettke, T. (2011). Loss of trace elements from serpentinites during fluid-assisted transformation of chrysotile to antigorite—An example from Guatemala. *Chemical Geology* **284**, 351–362.

Kohls, S. W. & Rodda, J. L. (1967). Iowaite, a new hydrous magnesium hydroxide–ferric oxychloride from the Precambrian of Iowa. *American Mineralogist* **52**, 1261–1271.

Krawczyk-Bärsch, E., Arnold, T., Reuther, H., Brandt, F., Bosbach, D. & Bernhard, G. (2004). Formation of secondary Fe-oxyhydroxide phases during the dissolution of chlorite—effects on uranium sorption. *Applied Geochemistry* **19**, 1403–1412.

Kretz, R. (1983). Symbols for rock-forming minerals. *American Mineralogist* **68**, 277–279.

Lee, C.-T. A., Oka, M., Luffi, P. & Agranier, A. (2008). Internal distribution of Li and B in serpentinites from the Feather River Ophiolite, California, based on laser ablation inductively coupled plasma mass spectrometry. *Geochemistry, Geophysics, Geosystems* **9**, doi:10.1029/2008GC002078.

Li, Z.-X. A. & Lee, C.-T. A. (2006). Geochemical investigation of serpentinized oceanic lithospheric mantle in the Feather River Ophiolite, California: Implications for the recycling rate of water by subduction. *Chemical Geology* **235**, 161–185.

Longerich, H. P., Jackson, S. E. & Günther, D. (1996). Laser ablation inductively coupled plasma mass spectrometric transient signal data acquisition and analyte concentration calculation. *Journal of Analytical Atomic Spectrometry* **11**, 899–904.

Ludwig, K. A., Kelley, D. S., Butterfield, D. A., Nelson, B. K. & Früh-Green, G. (2006). Formation and evolution of carbonate chimneys at the Lost City Hydrothermal Field. *Geochimica et Cosmochimica Acta* **70**, 3625–3645.

Martin, B. & Fyfe, W. S. (1970). Some experimental and theoretical observations on the kinetics of hydration reactions with particular reference to serpentinization. *Chemical Geology* **6**, 185–202.

McCollom, T. M. & Bach, W. (2009). Thermodynamic constraints on hydrogen generation during serpentinization of ultramafic rocks. *Geochimica et Cosmochimica Acta* **73**, 856–875.

McDonough, W. F. & Sun, S.-S. (1995). The composition of the Earth. *Chemical Geology* **120**, 223–253.

Menzies, M. A., Long, A., Ingram, G., Tatnell, M. & Janecky, D. (1993). MORB peridotite–sea water interaction: experimental constraints on the behaviour of trace elements, $^{87}Sr/^{86}Sr$ and $^{143}Nd/^{144}Nd$ ratios. In: Prichard, H. M., Alabaster, T., Harris, N. B. W. & Neary, C. R. (eds) *Magmatic Processes and Plate Tectonics. Geological Society, 76*. London: Special Publications, pp. 309–322.

Mercier, J.-C. C. & Nicolas, A. (1975). Textures and fabrics of upper-mantle peridotites as illustrated by xenoliths from basalts. *Journal of Petrology* **16**, 454–487.

Mével, C. (2003). Serpentinization of abyssal peridotites at mid-ocean ridges. *Comptes Rendus Géosciences* **335**, 825–852.

Michard, A. (1989). Rare earth element systematics in hydrothermal fluids. *Geochimica et Cosmochimica Acta* **53**, 745–750.

Milliken, K. L. & Morgan, J. K. (1996). Chemical evidence for near-seafloor precipitation of calcite in serpentinites (Site 897) and serpentinite breccias (Site 899), Iberia Abyssal Plain. In: Whitmarsh, R. B., Sawyer, D. S., Klaus, A. & Masson, D. G.

(eds) *Proceedings of the Ocean Drilling Program, Scientific Results, 149*. College Station, TX: Ocean Drilling Program, pp. 553–558.

Molina, J. F. & Poli, S. (2000). Carbonate stability and fluid composition in subducted oceanic crust: an experimental study on H_2O–CO_2-bearing basalts. *Earth and Planetary Science Letters* **176**, 295–310.

Molnár, G. L., Révay, Zs., Paul, R. L. & Lindstrom, R. M. (1998). Prompt-gamma activation analysis using the k_0 approach. *Journal of Radioanalytical and Nuclear Chemistry* **234**, 21–26.

Moriguti, T., Shibata, T. & Nakamura, E. (2004). Lithium, boron and lead isotope and trace element systematics of Quaternary basaltic volcanic rocks in northeastern Japan: mineralogical controls on slab-derived fluid composition. *Chemical Geology* **212**, 81–100.

Morishita, T., Hara, K., Nakamura, K., Sawaguchi, T., Tamura, A., Arai, S., Okino, K., Takai, K. & Kumagai, H. (2009). Igneous, alteration and exhumation processes recorded in abyssal peridotites and related fault rocks from an oceanic core complex along the Central Indian Ridge. *Journal of Petrology* **50**, 1299–1325.

Mottl, M. J., Wheat, C. G., Fryer, P., Gharib, J. & Martin, J. B. (2004). Chemistry of springs across the Mariana forearc shows progressive devolatilization of the subducting plate. *Geochimica et Cosmochimica Acta* **68**, 4915–4933.

Müntener, O., Pettke, T., Desmurs, L., Meier, M. & Schaltegger, U. (2004). Refertilization of mantle peridotite in embryonic ocean basins: trace element and Nd isotopic evidence and implications for crust–mantle relationships. *Earth and Planetary Science Letters* **221**, 293–308.

Niu, Y. (2004). Bulk-rock major and trace element compositions of abyssal peridotites: implications for mantle melting, melt extraction and post-melting processes beneath mid-ocean ridges. *Journal of Petrology* **45**, 2423–2458.

Noll, P. D., Newsom, H. E., Leeman, W. P. & Ryan, J. G. (1996). The role of hydrothermal fluids in the production of subduction zone magmas: Evidence from siderophile and chalcophile trace elements and boron. *Geochimica et Cosmochimica Acta* **60**, 587–611.

Palandri, J. L. & Reed, M. H. (2004). Geochemical models of metasomatism in ultramafic systems: Serpentinization, rodingitization, and sea floor carbonate chimney precipitation. *Geochimica et Cosmochimica Acta* **68**, 1115–1133.

Parkinson, I. J. & Pearce, J. A. (1998). Peridotites from the Izu–Bonin–Mariana forearc (ODP Leg 125): Evidence for mantle melting and melt–mantle interaction in a supra-subduction zone setting. *Journal of Petrology* **39**, 1577–1618.

Paulick, H., Bach, W., Godard, M., De Hoog, J. C. M., Suhr, G. & Harvey, J. (2006). Geochemistry of abyssal peridotites (Mid-Atlantic Ridge, 15°20'N, ODP Leg 209): Implications for fluid/rock interaction in slow spreading environments. *Chemical Geology* **234**, 179–210.

Plank, T. & Langmuir, C. H. (1998). The chemical composition of subducting sediment and its consequences for the crust and mantle. *Chemical Geology* **145**, 325–394.

Ranero, C. R. & Sallarés, V. (2004). Geophysical evidence for hydration of the crust and mantle of the Nazca plate during bending at the north Chile trench. *Geology* **32**, 549–552.

Ranero, C. R., Phipps Morgan, J., McIntosh, K. & Reichert, C. (2003). Bending-related faulting and mantle serpentinization at the Middle America trench. *Nature* **425**, 367–373.

Reeder, R. J., Nugent, M., Lamble, G. M., Tait, C. D. & Morris, D. E. (2000). Uranyl incorporation into calcite and aragonite: XAFS and luminescence studies. *Environmental Science and Technology* **34**, 638–644.

Révay, Zs. (2006). Calculation of uncertainties in prompt gamma activation analysis. *Nuclear Instruments and Methods in Physics Research A* **564**, 688–697.

Révay, Zs. (2009). Determining elemental composition using prompt γ activation analysis. *Analytical Chemistry* **81**, 6851–6859.

Révay, Zs., Molnár, G. L., Belgya, T., Kasztovszky, Zs. & Firestone, R. B. (2001). A new gamma-ray spectrum catalog and library for PGAA. *Journal of Radioanalytical and Nuclear Chemistry* **248**, 395–399.

Rinaudo, C., Gastaldi, D. & Belluso, E. (2003). Characterization of chrysotile, antigorite and lizardite by FT-Raman spectroscopy. *Canadian Mineralogist* **41**, 883–890.

Robertson, A. H. F. (2007). Evidence of continental breakup from the Newfoundland rifted margin (Ocean Drilling Program Leg 210): Lower Cretaceous seafloor formed by exhumation of subcontinental mantle lithosphere and the transition to seafloor spreading. In: Tucholke, B. E., Sibuet, J.-C. & Klaus, A. (eds) *Proceedings of the Ocean Drilling Program, Scientific Results, 210*. College Station, TX: Ocean Drilling Program, doi:10.2973/odp.proc.sr.210.104.2007.

Rucklidge, J. C. & Patterson, G. C. (1977). The role of chlorine in serpentinization. *Contributions to Mineralogy and Petrology* **65**, 39–44.

Salters, V. J. M. & Stracke, A. (2004). Composition of the depleted mantle. *Geochemistry, Geophysics, Geosystems* **5**, doi:10.1029/2003GC000597.

Sano, S. & Kimura, J.-I. (2007). Clinopyroxene REE geochemistry of the Red Hills Peridotite, New Zealand: interpretation of magmatic processes in the upper mantle and in the Moho transition zone. *Journal of Petrology* **48**, 113–139.

Savov, I. P., Ryan, J. G., D'Antonio, M., Kelley, K. & Mattie, P. (2005*a*). Geochemistry of serpentinized peridotites from the Mariana Forearc Conical Seamount, ODP Leg 125: Implications for the elemental recycling at subduction zones. *Geochemistry, Geophysics, Geosystems* **6**, doi:10.1029/2004GC000777.

Savov, I. P., Guggino, S., Ryan, J. G., Fryer, P. & Mottl, M. J. (2005*b*). Geochemistry of muds and metamorphic rocks from the Mariana Forearc, ODP Sites 1200 and 778–779, South Chamorro and Conical Seamounts. In: Shinohara, M., Salisbury, M. H. & Richter, C. (eds) *Proceedings of the Ocean Drilling Program, Scientific Results, 195*. College Station, TX: Ocean Drilling Program, doi:10.2973/odp.proc.sr.195.103.2005.

Savov, I. P., Ryan, J. G., D'Antonio, M. & Fryer, P. (2007). Shallow slab fluid release across and along the Mariana arc–basin system: Insights from geochemistry of serpentinized peridotites from the Mariana Forearc. *Journal of Geophysical Research, Solid Earth* **112**, B09205, doi:10.1029/2006JB004749.

Scambelluri, M., Piccardo, G. B., Philippot, P., Robbiano, A. & Negretti, L. (1997). High salinity fluid inclusions formed from recycled seawater in deeply subducted alpine serpentinite. *Earth and Planetary Science Letters* **148**, 485–499.

Scambelluri, M., Fiebig, J., Malaspina, N., Müntener, O. & Pettke, T. (2004). Serpentinite subduction: implications for fluid processes and trace-element recycling. *International Geology Review* **46**, 595–613.

Schmidt, K., Koschinsky, A., Garbe-Schönberg, D., de Carvalho, L. M. & Seifert, R. (2007). Geochemistry of hydrothermal fluids from the ultramafic-hosted Logatchev hydrothermal field, 15°N on the Mid-Atlantic Ridge: Temporal and spatial investigation. *Chemical Geology* **242**, 1–21.

Seifert, K. & Brunotte, D. (1996). Geochemistry of serpentinized mantle peridotite from site 897 in the Iberia Abyssal Plain. In: Whitmarsh, R. B., Sawyer, D. S., Klaus, A. & Masson, D. G. (eds) Proceedings of the Ocean Drilling Program, *Scientific Results, 149*. College Station, TX: Ocean Drilling Program, pp. 413–424.

Seitz, H.-M. & Woodland, A. B. (2000). The distribution of lithium in peridotitic and pyroxenitic mantle lithologies — an indicator of magmatic and metasomatic processes. *Chemical Geology* **166**, 47–64.

Seyler, M., Lorand, J.-P., Dick, H. J. B & Drouin, M. (2007). Pervasive melt percolation reactions in ultra-depleted refractory harzburgites at the Mid-Atlantic Ridge, 15°20'N: ODP Hole 1274A. *Contributions to Mineralogy and Petrology* **153**, 303–319.

Sharp, Z. D. & Barnes, J. D. (2004). Water-soluble chlorides in massive seafloor serpentinites: a source of chloride in subduction zones. *Earth and Planetary Science Letters* **226**, 243–254.

Sims, K. W. W., Newsom, H. E. & Gladney, E. S. (1990). Chemical fractionation during formation of the Earth's core and continental crust: clues from As, Sb, W, and Mo. In: Newsom, H. E. & Jones, J. H. (eds) *Origin of the Earth*. New York: Oxford University Press, pp. 291–317.

Singer, B. S., Jicha, B. R., Leeman, W. P., Rogers, N. W., Thirlwall, M. F., Ryan, J. & Nikolaysen, K. E. (2007). Along-strike trace element and isotopic variation in Aleutian Island arc basalt: Subduction melts sediments and dehydrates serpentine. *Journal of Geophysical Research* **112**, B06206, doi:10.1029/2006JB004897.

Singer, D. M., Maher, K. & Brown, G. E., Jr (2009). Uranyl–chlorite sorption/desorption: Evaluation of different U(VI) sequestration processes. *Geochimica et Cosmochimica Acta* **73**, 5989–6007.

Skelton, A. D. L. & Valley, J. W. (2000). The relative timing of serpentinisation and mantle exhumation at the ocean–continent transition, Iberia: constraints from oxygen isotopes. *Earth and Planetary Science Letters* **178**, 327–338.

Snow, J. E. & Dick, H. J. B. (1995). Pervasive magnesium loss by marine weathering of peridotite. *Geochimica et Cosmochimica Acta* **59**, 4219–4235.

Stephens, C. J. (1997). Heterogeneity of oceanic peridotite from the western canyon wall at MARK: results from site 920. In: Karson, J. A., Cannat, M., Miller, D. J. & Elthon, D. (eds) *Proceedings of the Ocean Drilling Program, Scientific Results, 153*. College Station, TX: Ocean Drilling Program, pp. 285–303.

Tatsumi, Y. (1989). Migration of fluid phases and genesis of basalt magmas in subduction zones. *Journal of Geophysical Research* **94(B4)**, 4697–4707.

Tonarini, S., Agostini, S., Doglioni, C., Innocenti, F. & Manetti, P. (2007). Evidence for serpentinite fluid in convergent margin systems: The example of El Salvador (Central America) arc lavas. Geochemistry, *Geophysics, Geosystems* **8**, doi:10.1029/2006GC001508.

Ulmer, P. & Trommsdorff, V. (1995). Serpentine stability to mantle depths and subduction-related magmatism. *Science* **268**, 858–861.

Vils, F., Pelletier, L., Kalt, A., Müntener, O. & Ludwig, T. (2008). The lithium, boron and beryllium content of serpentinized peridotites from ODP Leg 209 (Sites 1272A and 1274A): implications for lithium and boron budgets of oceanic lithosphere. *Geochimica et Cosmochimica Acta* **72**, 5475–5504.

Wicks, F. J. & Whittaker, E. J. W. (1977). Serpentine textures and serpentinization. *Canadian Mineralogist* **15**, 459–488.

Wicks, F. J., Whittaker, E. J. W. & Zussman, J. (1977). An idealized model for serpentine textures after olivine. *Canadian Mineralogist* **15**, 446–458.

Witt-Eickschen, G. & O'Neill, H. StC. (2005). The effect of temperature on the equilibrium distribution of trace elements between clinopyroxene, orthopyroxene, olivine and spinel in upper mantle peridotite. *Chemical Geology* **221**, 65–101.

Wunder, B., Deschamps, F., Watenphul, A., Guillot, S., Meixner, A., Romer, R. L. & Wirth, R. (2010). The effect of chrysotile nanotubes on the serpentine–fluid Li-isotopic fractionation. *Contributions to Mineralogy and Petrology* **159**, 781–790.

You, C.-F., Castillo, P. R., Gieskes, J. M., Chan, L. H. & Spivack, A. J. (1996). Trace element behavior in hydrothermal experiments: Implications for fluid processes at shallow depths in subduction zones. *Earth and Planetary Science Letters* **140**, 41–52.